

# On the Galactic radio signal from stimulated decay of axion dark matter

P. S. Bhupal Dev, Francesc Ferrer, and Takuya Okawa\*

*Department of Physics and McDonnell Center for the Space Sciences,  
Washington University, Saint Louis, MO 63130, USA*

## Abstract

We study the full-sky distribution of the radio emission from the stimulated decay of axions which are assumed to compose the dark matter in the Galaxy. Besides the constant extragalactic and CMB components, the decays are stimulated by a Galactic radio emission with a spatial distribution that we empirically determine from observations. We compare the diffuse emission to the counterimages of the brightest supernovæ remnants, and take into account the effects of free-free absorption. We show that, if the dark matter halo is described by a cuspy NFW profile, the expected signal from the Galactic center is the strongest. Interestingly, the emission from the Galactic anti-center provides competitive constraints that do not depend on assumptions on the uncertain dark matter density in the inner region. Furthermore, the anti-center of the Galaxy is the brightest spot if the Galactic dark matter density follows a cored profile. The expected signal from stimulated decays of axions of mass  $m_a \sim 10^{-6}$  eV is within reach of the Square Kilometer Array for an axion-photon coupling  $g_{a\gamma} \gtrsim (2-3) \times 10^{-11} \text{ GeV}^{-1}$ .

## 1 Introduction

The axion was originally introduced to address the strong CP problem in quantum chromodynamics (QCD) [1–3]. The QCD axion emerges as a pseudo-Nambu-Goldstone boson (pNGB) when the  $U(1)_{\text{PQ}}$  symmetry is broken. It can also be a viable cold dark matter candidate [4–7]. These considerations have been extended to axion-like particles (ALPs), i.e. pseudoscalar particles that could generically appear as pNGBs in theories with a spontaneously broken global  $U(1)$  symmetry, which are ubiquitous in string-inspired beyond the Standard Model (SM) constructions [8, 9]. ALPs cover a much broader mass-coupling range than the original QCD axion [10], and have inspired many novel laboratory and astrophysical searches [11, 12].

A common characteristic of the QCD axion, as well as of ALPs, is that their couplings to the SM particles are suppressed by inverse powers of the  $U(1)$  symmetry breaking scale,  $f_a$ . In this paper, we will only consider the ALP coupling to photons (or electromagnetic fields) which can be parametrized by the following Lagrangian:

$$-\mathcal{L} = \frac{1}{2}m_a^2 a^2 - \frac{g_{a\gamma}}{4} a F_{\mu\nu} \tilde{F}^{\mu\nu} = \frac{1}{2}m_a^2 a^2 + g_{a\gamma} a \mathbf{E} \cdot \mathbf{B}, \quad (1)$$

where  $F_{\mu\nu}$  is the electromagnetic field strength tensor,  $\tilde{F}^{\mu\nu}$  is its dual,  $a$  is the axion field, and  $\mathbf{E}$  and  $\mathbf{B}$  are the electric and magnetic fields, respectively. The effective axion-photon coupling  $g_{a\gamma}$  has the dimension of inverse mass; specifically, for the QCD axion,  $g_{a\gamma} = \alpha C_{a\gamma} / (2\pi f_a)$ , where  $\alpha$  is the electromagnetic coupling strength and  $C_{a\gamma}$  is a model-dependent dimensionless quantity typically of order unity; e.g. in the Kim-Shifman-Vainshtein-Zakharov (KSVZ) [13, 14] model,  $C_{a\gamma} = -0.97$ , and in the Dine-Fischler-Srednicki-Zhitnitsky (DFSZ) [15, 16] and all grand-unified axion models,  $C_{a\gamma} = 0.36$ . Moreover, the QCD axion mass satisfies the relation  $m_a f_a \approx m_\pi f_\pi$ , where  $m_\pi$  and  $f_\pi$  are the pion mass and pion decay

---

\*o.takuya@wustl.edu

constant, respectively. Including QED and NNLO corrections in chiral perturbation theory leads to the relation [17]

$$m_a = 5.691(51)\mu\text{eV} \left( \frac{10^{12} \text{ GeV}}{f_a} \right), \quad (2)$$

thus restricting  $m_a$  and  $g_{a\gamma}$  to a narrow band. However, in general, the ALP mass  $m_a$  and coupling  $g_{a\gamma}$  are treated as independent free parameters, and the experimental constraints are often quoted in the  $(m_a, g_{a\gamma})$  plane.

As alluded to above, QCD axions or ALPs may also account for the dark matter in the Universe. They could be produced in the early Universe by several mechanisms [18, 19], such as vacuum misalignment [4–6], thermal production [20–23], collapse of cosmic strings and domain walls [24–28], decay of heavier particles (e.g. moduli or inflaton coupling to axions) [29–35] and Hawking radiation from primordial black holes [36–38]. For instance, in the misalignment mechanism, the induction of nonzero QCD axion mass by non-perturbative QCD instanton effects at around the QCD phase transition  $T \sim \Lambda_{\text{QCD}}$  triggers oscillations of the axion field that could yield the required amount of the dark matter in the Universe for QCD axions in mass range  $m_a \sim \mu\text{eV}$ , which is our main focus here.

Multiple lines of reasoning have been considered in the literature to constrain the parameter space of ALPs in the  $\mu\text{eV}$  mass region [39]. The coupling to electromagnetic fields causes the conversion of axions into photons in the presence of an external magnetic field [40]. Haloscopes such as the Axion Dark Matter eXperiment (ADMX) [41–44] use a strong magnetic field applied inside a resonant cavity to find evidence of the conversion of axions to photons in the Galactic dark matter halo. Assuming that axions compose all the dark matter, the absence of a signal at ADMX puts an upper bound on the axion-photon coupling  $g_{a\gamma} \lesssim 3 \times 10^{-16} \text{ GeV}^{-1}$  (at 90% confidence level (C.L.)) in the  $\mu\text{eV}$  mass range and already excludes both KSVZ and DFSZ models over a narrow mass range of  $2.8 - 4.2 \mu\text{eV}$  [42, 43].

The same coupling also induces the production of axions from photons inside stellar objects. Helioscopes like the CERN Axion Solar Telescope (CAST) [45] searched for axions from the Sun, and placed a bound on  $g_{a\gamma} < 6.63 \times 10^{-11} \text{ GeV}^{-1}$  (at 95% C.L.) for axions with mass  $m_a \lesssim 0.02 \text{ eV}$ , which remains one of the most stringent laboratory constraints on ALPs in a wide mass range.

Axions can also be searched for by considering astrophysical processes. Axion-photon conversion inside stellar cores affects the ratio of horizontal branch stars to red giants ( $R$  parameter). An analysis of 39 Galactic globular clusters gave  $g_{a\gamma} < 6.54 \times 10^{-11} \text{ GeV}^{-1}$  (95% C.L.) for  $m_a \lesssim 100 \text{ keV}$  [46]. This was recently updated to  $g_{a\gamma} < 4.7 \times 10^{-11} \text{ GeV}^{-1}$  (95% C.L.) from the observed ratio of asymptotic giant branch to horizontal branch stars ( $R_2$  parameter) using a semiconvective mixing scheme [47]. Using the predictive mixing convective boundary scheme, as favored by asteroseismological evidence, improves the bound to  $g_{a\gamma} < 3.4 \times 10^{-11} \text{ GeV}^{-1}$  [47].

Similarly, axion DM may efficiently convert to photons in the magnetospheres of neutron stars, producing nearly monochromatic radio emission. Using archival Green Bank Telescope data collected in a survey of the Galactic Center in the C-Band by the Breakthrough Listen project, constraints on  $g_{a\gamma}$  down to the level of  $10^{-11} \text{ GeV}^{-1}$  was set for axion DM masses between 15 and 35  $\mu\text{eV}$  [48]. Another study that does not rely on axions being the DM uses the fact that axions can be copiously produced in localized regions (polar caps) of neutron star magnetospheres from the spacetime oscillations of  $\mathbf{E} \cdot \mathbf{B}$ , and their resonant conversion into photons can generate a large broadband contribution to the neutron star’s intrinsic radio flux [49]. Comparing observations of 27 nearby pulsars to predictions from sophisticated particle-in-cell simulations, an upper limit of  $g_{a\gamma} \lesssim (2 - 10) \times 10^{-12} \text{ GeV}^{-1}$  (95% C.L.) was obtained for  $10^{-9} \lesssim m_a/\text{eV} \lesssim 10^{-5}$  [50].

Given the current constraints, QCD axions with a mass  $\sim \mu\text{eV}$  interact with the electromagnetic field very weakly. Thus, their spontaneous decay rate to two photons in vacuum is extremely small:

$$\tau_a = \frac{64\pi}{g_{a\gamma}^2 m_a^3} \simeq 10^{43} \text{ s} \left( \frac{10^{-10} \text{ GeV}^{-1}}{g_{a\gamma}} \right)^2 \left( \frac{1 \mu\text{eV}}{m_a} \right)^3. \quad (3)$$

This tiny decay rate makes it difficult to search QCD axions by photon signals from their spontaneous decay.<sup>1</sup> However, the decay rate can be enhanced (by several orders of magnitude) in the presence of ambient photons since electromagnetic fields with an energy equivalent to half of ALP mass can stimulate decays of ALPs into two photons, which are emitted back-to-back in the rest frame of ALPs [53]. Thus, the incident wave of photons is amplified in the forward direction and reflected in the opposite direction [53–56]. This phenomenon could generate an observable amplification of radio signals from different astrophysical targets, such as dwarf spheroidal Galaxies, the Galactic Center and halo, and Galaxy clusters [57, 58]. We can also observe photons produced from stimulated decay of ALPs in the exact opposite direction (antipodal point) to a bright astrophysical source in the rest frame of the axion. This counterimage, dubbed as *gegenschein*, has been studied for bright radio sources, such as Cygnus A [59] and supernova remnants (SNRs) [60, 61]. This *gegenschein* signal, obtained by integrating over all the axion decay in a DM column oriented along the line of sight, can in principle be detected using powerful radio telescopes, like the current Five-hundred-meter Aperture Spherical radio Telescope (FAST) [62] or the future Square Kilometer Array (SKA) [63]. It will provide yet another probe of the axion-photon coupling  $g_{a\gamma}$  in the  $\mu\text{eV}$  ALP mass range, which falls right in the frequency range of operation of the radio telescopes:

$$\nu_a = \frac{m_a}{4\pi} \simeq 0.1 \text{ GHz} \left( \frac{m_a}{1 \mu\text{eV}} \right). \quad (4)$$

In this study, we carefully scrutinize the radio signals from stimulated decays of axions and include a number of effects previously not considered. We take into account the photon absorption due to electrons in the Galaxy that could potentially affect the observed signal. We construct an all-sky map of the signal-to-noise ratio at different radio frequencies. In addition to the three brightest SNRs considered previously, we include a fourth SNR S147 (whose counterimage will be close to the Galactic Center), and also include the effect of SNR parameter uncertainties on the signal. The effect of DM density profile (cuspy versus cored) on the radio signal is also studied. We find that at high frequencies ( $> \text{GHz}$ ), the strongest signal is from the Galactic Center for both cuspy and cored profiles, whereas at low frequencies, the strongest signal is from either Galactic Center or Anti-center, depending on whether the density profile is cuspy or cored at the Center. Similarly, among the four point sources considered, S147 gives us the best limit for the cuspy profile. The sensitivities obtained here are comparable to the existing limits, and those from the Galactic Anti-center are especially robust against astrophysical uncertainties. Finally, we also quantify the potential effects of axion miniclusters and mass segregation due to dynamical friction on the radio signal, and find that their effect on the signal flux is negligible (at most 0.3%).

The rest of the paper is structured as follows: in Section 2 we review the calculation of the photon flux from the stimulated decay of axions (with additional details reported in Appendix A) and we discuss some factors overlooked before that may affect the signal observed at the Earth. Section 3 describes the Galactic environment and the characteristics of the SNRs considered here. The specifications of the relevant telescopes used in this analysis are summarized in Section 4. The results are discussed in Section 5. Our conclusions are given in Section 6.

## 2 Radio signal from the stimulated decay of axion dark matter

Let us consider a bright radio source such as an SNR in the galaxy or a powerful extragalactic source like Cygnus A. The beam of radio photons may induce the stimulated decay of axions on its way through the Galactic DM halo to the Earth and beyond. The *gegenschein* signal [59] is generated along the continuation of the line of sight to the source, but to the direction opposite to the source. This could be a clean signal if there is no other bright source in the opposite direction of the original bright source in

---

<sup>1</sup>This is unlike other decaying DM candidates, like keV sterile neutrinos [51], or heavy decaying DM [52], where the photon signal constitutes one of the main probes.

the sky. In contrast, the stimulated signal generated along the line of sight in the same direction as the original source will be difficult to isolate from the bright continuum background of the source itself.

The observed photon flux has contributions from the decay of axions at a distance  $r$  away from the Earth that occurred at  $t - r/c$ , and was stimulated by a photon that had passed the current location of the Earth at time  $t - 2r/c$ , where  $c$  is the speed of light in vacuum.<sup>2</sup> If the radio source was significantly brighter in the past, as expected for some SNRs [60, 61], it could generate a striking bright image in the opposite direction, which is the *gegenschein* signal, whose frequency is set by the axion mass.

The flux density of photons from stimulated decays of axions averaged over the photon bandwidth  $\Delta\nu$  is given by (see Appendix A for the detailed derivation)

$$S_\nu = \frac{\Gamma_a}{4\pi\Delta\nu} \int dx \int d\Omega \rho_a(x, \Omega) e^{-\tau(\nu_a, x, \Omega)} \left( f_\gamma(x, \Omega, t) + \tilde{f}_\gamma(x, \Omega, t) \right), \quad (5)$$

where  $\Gamma_a = \tau_a^{-1}$  is the spontaneous axion decay rate [cf. Eq. (3)],  $\rho_a$  is the axion mass density along the line of sight (which depends on the DM density profile),  $\tau$  is the optical depth (see below), and  $\nu_a$  is the frequency at which the signal peaks for a given axion mass  $m_a$  [cf. Eq. (4)]. Here, we integrate the solid angle  $\Omega$  over the field of view of the radio telescope under consideration. The distribution functions  $f_\gamma$  and  $\tilde{f}_\gamma$  correspond to photons moving towards and away from the Earth, respectively,<sup>3</sup> and their time dependence arises because of the time-dependent radio photons from point sources like SNRs. The radio photons from continuum sources, like the Galactic, extragalactic, and CMB emissions are treated as steady emissions (independent of time).

The exponential factor in Eq. (5) accounts for the fact that a fraction of the photons from axion decays will be absorbed before they can reach the Earth. This is mainly due to free-free absorption, which we model as a thermal plasma of ionized hydrogen uniformly mixed with the synchrotron-emitting relativistic gas. The absorption coefficient is given by [64, 65]

$$\kappa(\nu, \mathbf{x}) = (9.8 \times 10^{-3} \text{ cm}^{-1}) [n_e(\mathbf{x})]^2 [T_e(\mathbf{x})]^{-3/2} \nu^{-2} \left[ 19.8 + \ln \left( \frac{[T_e(\mathbf{x})]^{3/2}}{\nu} \right) \right], \quad (6)$$

where  $n_e(\mathbf{x})$  is the electron number density in units of  $\text{cm}^{-3}$ ,  $T_e(\mathbf{x})$  is the kinetic temperature of thermal electrons in K and  $\nu$  is the observing frequency in Hz. The optical depth  $\tau$  in Eq. (5) is obtained by integrating the absorption coefficient along the line of sight from the Earth to the point where the stimulated axion occurs:

$$\tau(\nu, x, \Omega) = \int_0^x dl \kappa(\nu, l, \Omega). \quad (7)$$

Note that Ref. [60] used an alternative form for  $\kappa$  by approximating the last term in brackets (Gaunt factor) in Eq. (6) by a simple power law in  $\nu$  and  $T_e$ . We use the exact expression (6) for reasons explained in Section 3.2.

So far we have implicitly assumed that both the DM and the observer on Earth are at rest in the frame of the Galaxy. In reality there are several factors that can affect the radio signal, especially when dealing with Galactic point sources [60, 61]:

- DM in the Galaxy has a non-zero velocity dispersion  $\sigma_a \approx 5 \times 10^{-4} c$  [66], and a lower value in colder structures such as dwarf Spheroidal satellites. As a result, axion decay does not occur at rest in the frame of the Galaxy and the photons do not point exactly along the line of sight from the Earth to a point source, but could deviate by an angle  $\theta$  up to  $\sigma_a$  [cf. Fig. 1]. Hence, point sources are smeared and the signal they generate would have a size  $2\psi \simeq 2\sigma_a(d_s + x)/d_s$ , where  $d_s$  is the

<sup>2</sup>We set  $c = 1$  elsewhere in the text, but keep it here for clarity.

<sup>3</sup>Our flux expression differs from Eq. (3.1) in Ref. [58] in the last term where we take into account the fact that the flux of photons traveling towards and away from the Earth may not necessarily be the same.

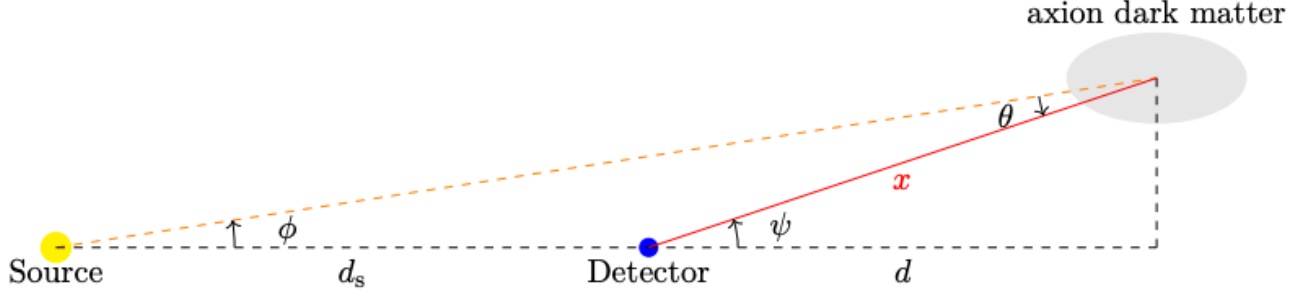


Figure 1: A schematic diagram (not to scale) of the stimulated decay of an axion. The radio photon from the source (dotted orange line) induces the stimulated decay of an axion in a DM cloud (the gray ellipse). Two back-to-back photons with energy equal to  $m_a/2$  are emitted in the rest frame of the axion, and one of them (solid red line) is detected by a radio telescope on Earth (the pale blue dot), located at a distance  $x$  from the point where axion decays. In the Galactic frame, the angle  $\theta$  could be as large as the axion velocity dispersion  $\sigma_a$ . Using trigonometric identities, we can estimate the deviation angle  $\psi \simeq \sigma_a(d_s + x)/d_s$ .

distance between the Earth and the source and  $x$  is that between the Earth and the point where the axion decays. This effect is mostly relevant for point sources, and not for diffuse signals. Moreover, we will use the radio telescopes in the single-dish mode, and therefore, we can ignore the smearing effect, unlike Refs. [60, 61] which use the interferometer mode where the angular size of the signal has to be carefully determined.

The motion of axions also broadens the signal in frequency space, and we choose the observation bandwidth to maximize the signal-to-noise ratio as discussed in Section 4.

- The peculiar motion of a radio source causes different effects on the image depending on whether the motion is along or perpendicular to our line of sight. For instance, the signal could shift from the current location of the source due to motion perpendicular to our line of sight. The deviation can be estimated from the aberration angle  $\theta_{\text{de}} \simeq d_p/d_s$ , where  $d_s$  is the distance to the source and  $d_p$  is the distance that the source travels during the relevant time to generate the signal.

For all the SNRs we consider here,  $\theta_{\text{de}} \lesssim 5$  arcmin, which is typically smaller than the angular resolution of the radio telescopes like SKA in the single dish mode [63], so the aberration effect will mostly cause the image of the SNR in the radio telescope to be blurred and enlarged by an order one factor. On the other hand, the motion of a source along our line of sight can reduce or enhance the flux, which is proportional to the inverse of the distance between the Earth and the source squared. This effect turns out to be negligible for SNRs [60] and for the Galactic center since the orbit of the solar system is approximately circular, and therefore, the distance to the source remains nearly constant.

- The shadow of the Earth might temporarily shield the radio photons from the source, which could either stop the stimulated decay of axions on the other side of Earth or prevent the photons from axion decays outside the shadow from passing the Earth. However, both effects turn out to be negligible due to the motion of the Earth in the DM rest frame [60].

### 3 The Galactic contribution

We would like to determine the contribution to the radio signal generated by the stimulated decay of DM axions within the Galaxy in any direction. To evaluate the flux we first have to specify the distribution

of the DM in the Galaxy, the density and the temperature of the electron plasma that contributes to the opacity, and the background radio photons that stimulate the decays of axions in the DM halo.

### 3.1 The mass density of the Milky Way

The mass distribution of the Galaxy is typically described as the superposition of different components: the bulge, the thin and thick disks, and the DM halo; see e.g. Refs. [67–69] for detailed models.

Numerical  $N$ -body simulations suggest that the density of the DM in the Galaxy, which we assume to be exclusively composed of ALPs, follows the so-called NFW profile [70]:

$$\rho_{\text{NFW}}(r) = \frac{\delta_c \rho_c}{(r/r_s)(1+r/r_s)^2}, \quad (8)$$

where  $r_s$  is the characteristic scale radius,  $\rho_c \equiv 3H_0/8\pi G \simeq 10^{-29} \text{ g cm}^{-3}$  is the critical density of the Universe ( $G$  being Newton’s constant and  $H_0$  the current Hubble parameter), and  $\delta_c$  is the overdensity parameter:

$$\delta_c = \frac{\Delta_{\text{vir}}}{3} \frac{C^3}{\ln(1+C) - C/(1+C)}, \quad (9)$$

where the concentration parameter  $C = R_{\text{vir}}/r_s$ , and the halo mass is normalized by the virialization radius  $R_{\text{vir}}$  that encloses a mass density  $\Delta_{\text{vir}} = 200\rho_c$ . A recent comparison of the dynamics of the Milky Way satellites with the predictions of Galaxy formation simulations [71] yields a total mass of the halo of the Galaxy  $M_{200}^{\text{MW}} = 1.17^{+0.21}_{-0.15} \times 10^{12} M_\odot$  (at 68% C.L.), and a concentration parameter of  $C_{200}^{\text{MW}} = 10.9^{+2.6}_{-2.0}$ , from which we can derive  $R_{\text{vir}} \simeq 221$  kpc and  $r_s \simeq 20$  kpc. From Eq. (8), this gives a local DM density of  $\rho_{\text{local}} \simeq 0.3 \text{ GeV cm}^{-3}$ .

However, several observations suggest that while the relatively massive Galaxies show a cuspy NFW-like (or generalized NFW) profile [72], a cored DM profile provides a better fit to the rotation curves of smaller galaxies [73–75]. For example, the best NFW fit to the observations of dwarf Spheroidal satellites of the Milky Way can be much less concentrated than expected from simulations [76], and mass estimates at different radii are consistent with cored potentials [77, 78]. Furthermore, baryonic physics processes such as stellar feedback are expected to alter the central DM distribution in larger Galaxies like the Milky Way [79]. Thus, in our calculations we also consider the possibility that the DM is described by a cored Burkert profile [80]:

$$\rho_{\text{Bur}}(r) = \frac{\rho_s}{\left(1 + \frac{r}{r_s}\right)\left(1 + \frac{r^2}{r_s^2}\right)}. \quad (10)$$

Agreement with mass estimates of the Galaxy and requiring that the local DM density is  $\rho_{\text{local}} \simeq 0.3 \text{ GeV cm}^{-3}$  determines the scale radius  $r_s \simeq 12.67$  kpc and the scale density  $\rho_s \simeq 0.712 \text{ GeV cm}^{-3}$  [81].

### 3.2 Electron number density in the Galaxy

As shown in Eq. (6), the absorption coefficient depends on the number density and temperature of electrons along the line of sight. Twelve models of the free electron distribution in the Milky Way are explored in Ref. [82], and their parameters are determined so that the observed distances of known pulsars are recovered from their observed dispersion measure. Most models can predict the dispersion measure within a factor of 1.5-2 for 75% of the lines of sight. For definiteness, we use the plane-parallel two-component model [83]<sup>4</sup>:

$$n_e(R, z) = n_0 \frac{f(R/R_0)}{f(R_\odot/R_0)} f\left(\frac{z}{z_0}\right) + n_1 \frac{f(R/R_1)}{f(R_\odot/R_1)} f\left(\frac{z}{z_1}\right) \quad (11)$$

<sup>4</sup>Choosing the TC93 model [84], which provides a better fit to the pulsar data, has a dependence on the Galactic coordinates, and significantly increases the computational costs, without altering the results much.



where  $R$  is the polar distance from the Galactic Center,  $R_\odot = 8.5$  kpc is the Galactocentric distance of the Sun, and  $z$  is the height above the Galactic mid-plane. We take the best-fit parameters from Table 4 in Ref. [82] for  $f(x) = \text{sech}^2(x)$ , i.e.,

$$n_0 = 1.77 \times 10^{-2} \text{ cm}^{-3}, \quad R_0 = 15.4 \text{ kpc}, \quad z_0 = 1.10 \text{ kpc}, \quad (12)$$

$$n_1 = 1.07 \times 10^{-2} \text{ cm}^{-3}, \quad R_1 = 3.6 \text{ kpc}, \quad z_1 = 0.04 \text{ kpc}. \quad (13)$$

We note that our calculation of the optical depth using the electron number density given above is different from Ref. [60], which used the emission measure,  $\text{EM} = \int n_e^2 dx$ , along the line of sight, with  $n_e$  modeled as a plane-parallel distribution with a single scale height [85, 86]. This approach makes the optical depth negligible for the entire range of frequencies they investigated. In our case, the optical depth is negligible only at higher frequencies ( $\gtrsim 500$  MHz), but is important at low frequencies, where we get the best sensitivities. Moreover, the single-plane model does not provide a good fit to the pulsar data [82]. Both models greatly underestimate the EM in the close vicinity of the Galactic Center, which has been estimated to be  $\sim 10^5 \text{ cm}^{-6} \text{ pc}$  [87], based on the radio observation of Sgr A\* and the 7 arcmin halo surrounding it. But the two component model gives  $\mathcal{O}(10^2) \text{ cm}^{-6} \text{ pc}$ , compared to  $\mathcal{O}(10^{-1}) \text{ cm}^{-6} \text{ pc}$  in the single-component model. See Section 5.1 on how we handle the EM discrepancy at the Galactic Center emission.

As for the electron temperature in Eq. (6), it can be derived from observations of radio recombination line and continuum emissions in H II regions. Taking a sample of 76 nebulae widely distributed over the Galactic disk, the best fit electron temperature in the Galaxy was found to be  $T_e = (5780 \pm 350) + (287 \pm 46)(R_{\text{gal}}/1 \text{ kpc})$  K, where  $R_{\text{gal}}$  is the Galactocentric distance [88]. Following Ref. [58], we will ignore the small temperature gradient in the Galactic disk and will assume a constant electron temperature  $T_e \sim 5000$  K.

### 3.3 Diffuse radio emission

As discussed in Section 2, the presence of a background of radio photons will stimulate the decay of DM axions, and the resulting flux of photons is linearly proportional to the occupation number  $f_\gamma$  of background photons. When estimating the diffuse emission from an arbitrary direction, we consider three separate contributions to  $f_\gamma$ : the cosmic microwave background (CMB), the extragalactic radio background (ERB), and the Galactic radio emission.

At higher frequencies ( $\gtrsim 10$  GHz), the main contribution to the photon background comes from the CMB. The spectrum is, hence, well approximated by a black-body spectrum:

$$f_{\gamma, \text{CMB}}(E_\gamma) = \frac{1}{e^{E_\gamma/k_B T_{\text{CMB}}} - 1}, \quad (14)$$

with  $T_{\text{CMB}} = 2.72548 \pm 0.00057$  K [89]. Here  $k_B$  is the Boltzmann constant.

Since extragalactic radio sources are likely to be distributed isotropically, the observed ERB is expected to be nearly isotropic. The analysis of radio maps with frequencies ranging from 22 MHz to 2.3 GHz provides a best fit to the brightness temperature of the isotropic extragalactic radio emission [90]:

$$T_{\text{exgal}}(\nu) \simeq 1.19 \text{ K} \left( \frac{1 \text{ GHz}}{\nu} \right)^{2.62}. \quad (15)$$

Then the stimulated enhancement factor can be obtained from the measured radio intensity:

$$f_\gamma(E_\gamma) = \frac{\pi^2 \rho_\gamma}{E_\gamma^3}, \quad (16)$$

where the energy density (which is same as the intensity up to a factor of  $c$ , the speed of light) can be written in terms of the brightness temperature as<sup>5</sup>

$$\rho_\gamma = \frac{2h\nu^3}{e^{h\nu/k_B T_b} - 1} \simeq 2\nu^2 k_B T_b \quad (\text{for } h\nu \ll k_B T). \quad (17)$$

For the frequency range of our interest,  $h\nu \ll k_B T_b$  holds for the extragalactic brightness temperature given in Eq. (15), because  $h\nu \sim m_a \sim \mu\text{eV}$ , whereas  $k_B T \sim 1 \text{ K} \sim 10^{-4} \text{ eV}$ .

From the above discussion, we see that both CMB and ERB sources contribute an isotropic radio background to the stimulated photon signal which only depends on the photon energy, or equivalently, on the axion mass. But the Galactic contribution to the radio background is more complicated, and depends on the Galactic coordinates of the line of sight. Radio photons are produced in the Galaxy via several processes including synchrotron radiation, thermal bremsstrahlung, and synchrotron self-absorption in SNRs. We estimate the Galactic contribution to  $f_\gamma$  from the observed brightness temperature  $T_{\text{gal}}$  of the 408 MHz Haslam map [91, 92]. Although the spectral index of the Galactic radio emission generally depends on the direction [93], we will use the ansatz given in Table 1 of Ref. [94] that was also used in Ref. [58]:

$$f_{\gamma, \text{gal}}(r, \nu) = f_{\gamma, \text{gal}}(r)|_{\nu=\nu_*} \times \begin{cases} (\nu/\nu_*)^{-3.173} & \nu < \nu_* \\ (\nu/\nu_*)^{-3.582} & \nu_* \leq \nu \leq 4.85 \text{ GHz} \\ 1.99(\nu/\nu_*)^{-4.14} & \nu > 4.85 \text{ GHz} \end{cases}, \quad (18)$$

which is obtained by fitting the observed radio flux from the inner  $2^\circ \times 1^\circ$  of the Galactic Center region at  $\nu_* = 1.415 \text{ GHz}$ .<sup>6</sup> As we will see in Section 5, the gegenschein signal induced by the diffuse emission from the Galactic Center (or Anti-center for low frequencies) give us better sensitivity than the point sources.

### 3.4 Radio emission from SNRs

Our objective is to determine the most favorable location in the sky to measure a potential radio signal associated with the stimulated decay of axion DM. Besides the diffuse emission (both direct and gegenschein) from the central region of the Galaxy, the gegenschein signal associated with bright point sources also stand out. SNRs are of particular interest, because they are known to be radio bright [95–97]. SNRs could emit a copious number of radio photons both thermally and non-thermally. Thermal radio emission consists of bremsstrahlung (free-free emission), photon emissions from charged particles accelerated by encountering another charged particle, radiative recombination continuum (free-bound emission), single photon emission due to the capture of a free electron by an ion, and two-photon emission from electrons in metastable states. Nonthermal emission includes synchrotron radiation caused by relativistic charged particles, mainly electrons and positrons, gyrating in a magnetic field and scattering between photons and cold electrons (Thomson scattering). Emissions due to synchrotron radiation are dominant in the radio frequencies of our interest and the photon spectrum follows a simple power law:  $S_\nu \propto E_\gamma^{-\alpha}$ , where the spectral index  $\alpha$  is typically around 0.5; see Table 1.

As implied by Eq. (5), a source that was brighter in the past could produce a brighter signal compared to its present state. As first proposed in Ref. [98], and summarized in [99, 100], the time evolution of SNRs can be roughly divided in four phases, namely, (i) Free expansion (or ejecta-dominated) phase, (ii) Adiabatic expansion (or Sedov-Taylor) phase, (iii) Radiative (or Snow-plough) phase, and (iv) Dispersion (or merging) phase. After a short initial free expansion phase that lasts a few hundred years, the bulk of the radio emission is generated in the early stages of the Sedov-Taylor or adiabatic phase. During this phase, which lasts  $\sim \mathcal{O}(\text{few} \times 10^4)$  years, the luminosity decreases steeply with time, so the total integrated gegenschein luminosity is expected to be much greater than what we would infer from the source's luminosity at present, since most of the radio emission was produced when the source was young.

<sup>5</sup>Here we keep the Planck's constant  $h$  for clarity, although elsewhere in the text, we have assumed  $\hbar \equiv h/2\pi = 1$ .

<sup>6</sup>Our Eq. (18) differs from Eq. (4.7) in Ref. [58] for  $\nu > 4.85 \text{ GHz}$  and ensures that  $f_{\gamma, \text{gal}}$  is continuous at  $\nu = 4.85 \text{ GHz}$ .



	S147	W28	Vela	W50
Distance [pc]	$1470^{+420}_{-270}$	$1900^{+300}_{-300}$	$287^{+19}_{-17}$	$50000^{+5000}_{-5000}$
Age [kyr]	$40^{+20}_{-10}$	$34.5^{+1.5}_{-1.5}$	$12^{+2}_{-2}$	$30^{+70}_{-10}$
Spectral index $\alpha$	$0.3^{+0.15}_{-0.15}$ ( $1.2^{+0.3}_{-0.3}$ )	$0.42^{+0.02}_{-0.02}$	$0.74^{+0.04}_{-0.04}$	$0.7^{+0.1}_{-0.2}$
Flux $S_\nu$ [Jy]	$59 \pm 6$	$310 \pm 20$	$610 \pm 105$	$85 \pm 20$
Galactic coordinates ( $l, b$ )	(180.0, $-1.7$ )	(6.4, $-0.1$ )	(263.9, $-3.3$ )	(39.7, $-2.0$ )
Size [arcmin]	180	48	255	60

Table 1: Parameters of the four SNRs used in this paper and the associated uncertainties [106, 107] (see also Ref. [61] and references therein). The spectral index of S147 depends on the frequency; the central value is 0.3 (1.2) for frequencies smaller (larger) than 1.7 GHz [110]. The fluxes are given at  $\nu = 1.7$  GHz for S147, and at  $\nu = 1$  GHz for the others. The flux uncertainties quoted here are based on the available measurements closest to 1 GHz.

The important SNR evolution parameters are the spectral index  $\alpha$ , magnetic field amplification (MFA) time  $t_{\text{MFA}}$ , and the age  $t_0$ . Following Ref. [61], we will consider two models for the evolution of the spectral index in the Sedov-Taylor phase, namely, (i)  $S_\nu \propto t^{-4\gamma/5}$  [101], and (ii)  $S_\nu \propto t^{-2(\gamma+1)/5}$  [102], where  $\gamma$  is the power law index for the differential energy spectrum of the synchrotron electrons:  $dn_e/dE_e \propto E_e^{-\gamma}$ , and is related to the spectral index of the photon flux by  $\gamma = 2\alpha + 1$  [103]. Thus,  $\gamma > 1$  (since  $\alpha > 0$ ), which implies the model (i) gives more optimistic flux. Similarly, for  $t_{\text{MFA}}$ , we will use the range of 30–300 years, with a central value of 100 years [104, 105].

Out of the roughly 300 Galactic SNRs recorded in Green’s catalog [106, 107], 60 of them have known distance, age and spectral index listed in the SNRcat catalog [108, 109]. Among these, the counterimage of W50 was found in Ref. [60] to yield the maximum signal-to-noise ratio in SKA 1, while Ref. [61] also considered Vela and W28. In our survey we add S147 to this list (see Table 1), because S147 (G180.0-1.7) is the closest SNR to the Galactic Anti-center, and therefore, its counterimage will be formed close to the Galactic Center. Although this counterimage is likely to be contaminated by radio photons from the Galactic Center, we still expect a large gegenschein flux from it since the flux from axion decay is proportional to the density of axions, which is the largest at the Galactic Center. Furthermore, S147 is the oldest of the four SNRs considered here, which enables its radio photons to stimulate decays of axions located far away from the Earth. Its spectral index varies depending on frequency: below 1.7 GHz, the spectrum is relatively flat, and the spectral index  $\alpha$  is estimated to be 0.3, while it grows to 1.2 above 1.7 GHz.

W28 (G6.4-0.1) is almost on the Galactic plane, but its counterimage would avoid being smeared by the radio background since it is away from the direction of the Galactic Center. It is encouraging that this SNR is almost as old as S147, and its observed flux at 1 GHz is large. On the other hand, Vela (G263.9-3.3) is a relatively young SNR, but it is the brightest among the four, even after excluding the radio photons from the pulsar nebula, and has a large spectral index, and thus, is expected to give a bright counterimage. Finally, W50 (G39.7-2.0) is the SNR with which Refs. [60, 61] place the strongest constraints on the axion-photon coupling  $g_{a\gamma}$ . It has a large spectral index, a relatively long age and is furthest away (among the four), which is a good combination that helps to generate a bright gegenschein image. As we will see in Section 5, S147 gives a slightly better constraint than the other three point sources considered before, but the diffuse emission from the Galactic Center and Anti-center give us the best constraints.

The SNR parameter values and uncertainties for the four point sources used in this study are taken from the Green’s catalog [107] and are summarized in Table 1.

### 3.5 Effects of small scale structure

Axion models where the PQ symmetry is broken after inflation generically predict that the DM distribution will be inhomogeneous at small scales. As a result, a fraction of the DM mass collapses into small halos called axion miniclusters [111–121]. Even denser axion stars [122–125] might form within miniclusters in a time shorter than the age of the Universe [126–129]. The presence of these inhomogeneities can give rise to striking effects [125, 130–139] and it is worth exploring whether their presence can also be revealed by their stimulated radio decays.

Since the precise abundance and distribution of axion stars is uncertain, we choose for our purposes a particular realization of the DM of the Galaxy where a fraction of order 10% of the DM mass is in the form of dilute axion stars with mass  $m_{\text{AS}}$  and radius [140]

$$R_a^{\text{dilute}} \sim 27000 \text{ km} \left( \frac{1 \text{ } \mu\text{eV}}{m_a} \right)^2 \left( \frac{10^{-12} M_\odot}{m_{\text{AS}}} \right). \quad (19)$$

In principle, the presence of such a clumpy component could give rise to statistical fluctuations of the radio signal along different lines of sight. However, the solid angle of the telescope beam corresponds to a DM column mass that is several orders of magnitude larger than the mass of the individual axion clumps [61]. For instance, for typical dilute star with radius given in Eq. (19) we would expect about  $10^{17}$  dilute stars along a given line of sight, so the tiny  $\sim 10^{-8}$  Poisson fluctuations are unobservable.

Moreover, since the signal from stimulated axion decay is proportional to the DM density, the presence of a clumpy component does not appear to change the observed flux (unlike e.g. an indirect signal from DM annihilation, which is proportional to the square of the density). This is indeed the case as long as the clumpy DM component has the same density distribution as the underlying homogeneous DM profile. However, if clumps are preferentially located e.g. at the outer parts of the halo compared to the homogeneous NFW or Burkert profile, the flux from stimulated axion decay would be different than the one expected from a completely smooth DM halo.

Since the spatial extent of axion miniclusters is small,  $\lesssim 1$  pc, and that of dilute stars is even smaller [cf. Eq. (19)], their initial mass distribution at the time the DM halo of the Galaxy was assembled is likely to coincide with that of the homogeneous halo. However, their distribution might be modified over time due to the effects of dynamical friction between ordinary stars and axion stars. Gravitational interactions between collisionless components lead to equipartition, where the average kinetic energy of the lighter component becomes equal to that of the heavier component [141–143]. This leads to mass segregation, where the more massive component (i.e. the ordinary star in this case) tends to drift closer to the cluster. Assuming that both axionic and ordinary stars follow a Maxwellian velocity distribution, the mean transferred energy is given by [144]

$$\frac{dE_{\text{AS}}}{dt} = \frac{\sqrt{96\pi} G^2 m_{\text{AS}} \rho_s \ln \Lambda}{[\langle v_s^2 \rangle + \langle v_{\text{AS}}^2 \rangle]^{3/2}} [m_s \langle v_s^2 \rangle - m_{\text{AS}} \langle v_{\text{AS}}^2 \rangle], \quad (20)$$

where subscripts denote either stars (s) or axion stars (AS),  $\langle v_s^2 \rangle$  and  $\langle v_{\text{AS}}^2 \rangle$  are the corresponding mean-squared velocities, and  $\rho_s = \rho_b + \rho_{\text{d,thin}} + \rho_{\text{d,thick}}$  is the density of ordinary stars which receives contributions from the bulge and from the thin and thick discs [67, 68]. We assume that the axion stars have the same velocity dispersion as that of the homogeneous component of the DM [66], which is comparable to velocity dispersion of stars in the Galaxy [145, 146], i.e.  $\langle v_s^2 \rangle \sim \langle v_{\text{AS}}^2 \rangle = \sigma_a^2 \simeq (5 \times 10^{-4} c)^2$ . The Coulomb logarithm in Eq. (20) is approximated by  $\ln \Lambda = \ln[d_{\text{max}} \sigma_a^2 / (G(m_s + m_{\text{AS}}))]$ , where  $d_{\text{max}}$  is an upper limit to the distance between a gravitationally interacting axion star and an ordinary star. A reasonable choice for  $d_{\text{max}}$  would be the bulge radius,  $r_b \simeq 2.1$  kpc. This gives  $\ln \Lambda = 23.1$ . We can now estimate the relaxation time  $t_{\text{relax}}$  as

$$t_{\text{relax}} \equiv \left| \frac{1}{\frac{1}{2} m_{\text{AS}} \langle v_{\text{AS}}^2 \rangle} \frac{d}{dt} \left( \frac{1}{2} m_{\text{AS}} \langle v_{\text{AS}}^2 \rangle \right) \right|^{-1} \simeq \frac{0.08 \sigma_a^3}{G^2 m_s \rho_s \ln \Lambda} \simeq 7000 \text{ Gyr} \left( \frac{100 M_\odot \text{pc}^{-3}}{\rho_s} \right) \left( \frac{M_\odot}{m_s} \right), \quad (21)$$

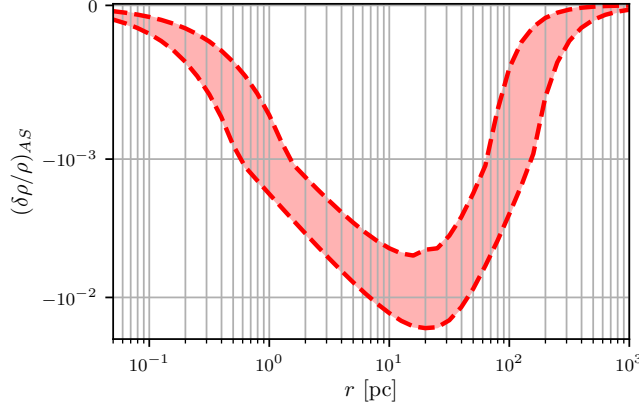


Figure 2: Mass deficit due to mass segregation between axion stars and ordinary stars as a function of distance from the Galactic Center. The band shows the uncertainty in the stellar mass density distribution in the Galaxy.

which turns out to be much longer than the age of the Universe for typical values of the stellar density in the bulge,  $\rho_s \simeq 100 M_\odot \text{pc}^{-3}$ , and a typical stellar mass of  $m_s \simeq 1 M_\odot$ . Hence, the mass segregation of axion stars and ordinary stars due to dynamical friction is an extremely slow process for the given mass hierarchy between ordinary and axionic stars.

In order to estimate the current distribution of axion stars, we further assume that the effect of mass segregation is spherically symmetric so that we can apply the virial theorem,  $E = -U/2$  (where  $E$  and  $U$  are the kinetic and potential energies respectively), to the system. Under these assumptions, the evolution of a radial mass shell is governed by the following differential equation [147]:

$$\frac{dr}{dt} = \frac{4\sqrt{2}\pi G^2 \rho_s m_s}{\sigma} \ln \Lambda \left( \frac{df(r)}{dr} \right)^{-1} \quad (22)$$

where  $f(r)$  is the gravitational potential energy per unit mass as a function of distance  $r$  from the Galactic Center. Here the gravitational potential is taken to be the sum of the contributions from the bulge, the thin disk, the thick disk, the axion stars, and the supermassive black hole at the Galactic Center with mass  $M_{\text{BH}} \approx 4 \times 10^6 M_\odot$  [148].

Figure 2 shows the mass density deficit  $(\delta\rho/\rho)_{\text{AS}} \equiv (\rho_{\text{AS}}(t) - \rho_{\text{AS}}(0))/\rho_{\text{AS}}(0)$  for the axion stars, calculated by solving Eq. (22), and taking  $\rho(t)/\rho(0) \simeq (r(0)/r(t))^3$  at  $t = 13.8$  Gyr, the current age of the Universe. We use two models to compute the mass deficit: For the optimistic model (lower curve) we set the stellar mass density  $\rho_s(r)$  to the value on the Galactic plane, whereas for the conservative model (upper curve) we take it equal to the value in the direction of the Galactic North (or South) pole. We see that the mass density of axion stars is reduced by at most 0.5% (conservative)-1.7% (optimistic) at  $r \sim 20$  pc from the Galactic Center. This will cause a reduction in the photon flux from stimulated axion decays by about 0.1% (conservative)-0.3% (optimistic). Thus, the mass segregation effect on the radio signal is negligible.

## 4 Radio telescopes

As shown in Eq. (4), the frequency of photons produced from stimulated axion decay naturally falls in the radio band for  $m_a \sim \mu\text{eV}$ , where the axion can make up the bulk of the DM. There are several radio telescopes that are currently operating, and even larger facilities will start collecting data in the next few years [149]. We here summarize the characteristics of FAST [62] (currently operating) and SKA [63]

	SKA1-low	SKA2-low	SKA1-mid	SKA2-mid	FAST
Frequency [MHz]	50-350	50-350	350-15400	350-50000	70-3000
$N_{\text{tele}}$	512	4800	197	2000	1
$D$ [m]	35	35	13.5, 15	13.5, 15	300
$\theta_{\text{res}}$ [deg]	12-1.7	12-1.7	4.0-0.91	4.0-0.28	1.0-0.023
$T_{\text{r}}$ [K]	40	40	20	20	20

Table 2: Main properties of the SKA [153] and FAST [154] relevant to our calculation.

(Phase 1 under construction and Phase 2 planned) as representative examples, which will be used to derive the sensitivity curves for the axion masses and couplings from the stimulated decay signal.

The Square Kilometer Array (SKA) [150] has one of the largest collecting areas among all radio telescopes. It comprises two different types of instruments, SKA-low and SKA-mid, that use dipole and parabolic antennas, respectively. SKA-low, located in Western Australia, observes radio photons with lower frequencies (50-350 MHz) and it consists of 512 telescopes, each with 35 m diameter and 256 antennas. SKA-mid, located in South Africa, is sensitive to photons with higher frequencies (350 MHz - 1.54 GHz, which will extend to 50 GHz with SKA2). It consists of 133 dishes with a diameter of 15 m and 64 MeerKAT dishes with a diameter of 13.5 m [151, 152]. On the other hand, FAST [62] is a single-dish telescope with a diameter of 300 m currently operating in China. Its design frequency range is from 70 MHz to 3 GHz, and up to 8 GHz with future upgrades. We summarize the specifications of these telescopes in Table 2.

Several key properties of a telescope enter the calculation of the axion decay signal: angular resolution, noise properties, bandwidth and frequency resolution. The angular resolution of a telescope with a diameter  $D$  is given by

$$\theta_{\text{res}} \simeq 1.22 \frac{\lambda}{D} \simeq 1.4^\circ \left( \frac{1 \text{ GHz}}{\nu} \right) \left( \frac{15 \text{ m}}{D} \right). \quad (23)$$

Given the resolution  $\theta_{\text{res}}$ , we can express the primary beam angular size as  $\Omega_{\text{pb}} = 2\pi (1 - \cos(\theta_{\text{res}}/2))$ .

The signal power in a bandwidth  $\Delta\nu$  observed by each antenna can be expressed as

$$P_{\text{signal}} = \eta A f_{\Delta} S_{\nu} \Delta\nu, \quad (24)$$

where  $S_{\nu}$  is the observed flux of radio photons in the bandwidth  $\Delta\nu$  [cf. Eq. (5)] with the integral over solid angle extending over the primary beam area,  $A = \pi(D/2)^2$  is the area of each dish,  $\eta$  is the detector efficiency which we set conservatively to 0.8 [63] for SKA and 0.7 for FAST [62].

Assuming that axion DM follows a Maxwell-Boltzmann velocity distribution, the signal-to-noise ratio is maximized for  $\Delta\nu = 2.17\nu_a\sigma_a$ , which contains a fraction  $f_{\Delta} = 0.721$  of all the photons from stimulated axion decays [59]. Our signal bandwidth  $\Delta\nu/\nu_a = 2.17\sigma_a \sim 10^{-3}$  is within the observable range of the radio telescopes considered here.

The instrument noise is characterized by the power

$$P_{\text{noise}} = 2k_B T \sqrt{\frac{\Delta\nu}{t_{\text{obs}}}}, \quad (25)$$

where  $t_{\text{obs}}$  is the observation time that we take to be 100 hours for definiteness.  $T = T_{\text{a}} + T_{\text{CMB}} + T_{\text{exgal}} + T_{\text{gal}} + T_{\text{r}}$  is the noise temperature which is the sum of contributions from atmospheric radio photons, CMB, extragalactic radio waves, Galactic radio emission, and the temperature of the receiver. The brightness temperature of the atmospheric signal is set to  $T_{\text{a}} = 3 \text{ K}$  [155]. The receiver temperature is  $T_{\text{r}} = 20 \text{ K}$  for FAST [62] and SKA-Mid, and 40 K for SKA-Low [63]. As discussed in Section 3.3 we take the frequency-dependent  $T_{\text{exgal}}$  from Eq. (15), and that of the Galactic emission is taken from the Haslam map [91, 92].

Putting things together, we find that the signal-to-noise ratio for a single telescope is given by

$$\left(\frac{S}{N}\right)_{\text{single}} = \frac{m_a^3 g_{a\gamma}^2}{512\pi^2} \frac{\eta A f_\Delta}{k_B T} \sqrt{\frac{t_{\text{obs}}}{\Delta\nu}} \sqrt{n_{\text{pol}}} \int dx \int d\Omega \rho_a(x, \Omega) e^{-\tau(\nu_a, x, \Omega)} \left(f_\gamma(x, \Omega, t) + \tilde{f}_\gamma(x, \Omega, t)\right), \quad (26)$$

where  $n_{\text{pol}} = 2$  is the number of polarizations of photons. If we now consider an array of  $N_{\text{tele}}$  telescopes, the signal-to-noise ratio is the root mean square of the signal-to-noise ratio of each telescope. Therefore,

$$\left(\frac{S}{N}\right)_{\text{array}} = \sqrt{N_{\text{ant}}} \left(\frac{S}{N}\right)_{\text{single}} \quad (27)$$

where  $N_{\text{ant}} = N_{\text{tele}} n_{\text{ant}}$  is the total number of antennas, i.e. the product of the number of telescopes and the number of antennas in each telescope.

A pair of telescope dishes can also work as an interferometer with an angular resolution  $\theta_{\text{pair}} \simeq \lambda/d_{\text{pair}}$  where  $d_{\text{pair}}$  is the spatial separation of the two dishes. In particular, the SKA telescope can be operated as a radio interferometer with  $N_{\text{tele}}(N_{\text{tele}} - 1)/2$  pairs of dishes. Each two-element interferometer contributes to the measurement when the angular size of the source  $\theta_{\text{source}}$  is smaller than the angular resolution  $\theta_{\text{pair}}$ . For larger sources, the visibility  $R \propto \sin q/q$  where  $q \equiv \pi\theta_{\text{source}}/\theta_{\text{pair}}$  becomes smaller and not all two-element interferometers contribute [103]. The maximum sensitivity is attained when all pairs of dishes function as interferometers. In general, the signal-to-noise ratio falls off like  $S/N \propto \sqrt{N_{\text{useable}}/N_{\text{pair}}}$  for extended sources where  $N_{\text{useable}}$  is the number of useable pairs.

For extended sources like the Galactic center, with angular size of  $\sim \mathcal{O}(1^\circ) \times \mathcal{O}(1^\circ)$ , single-dish mode is likely to achieve a larger signal-to-noise ratio. Even for SNRs, single dish mode gives better sensitivity [60] at lower frequencies. Thus, we will only use the single-dish mode for SKA.

## 5 Results

The non-observation of photons from the stimulated decays of axions in the Galactic DM halo can be used to place constraints on the axion-photon coupling  $g_{a\gamma}$ . For definiteness, we assume 100 hours of observation time and set the signal-to-noise ratio threshold  $(S/N)_{\text{array}} > 1$  to derive our sensitivity limits using FAST and SKA radio telescopes.

### 5.1 Sky maps

We generated all-sky maps of the expected diffuse flux of radio photons from stimulated decays of axions at three different frequencies: 50 MHz (the lowest frequency that SKA-low is sensitive to), 408 MHz (which matches the frequency of the Haslam map [91, 92]), and 1.54 GHz (the highest frequency that SKA-mid can reach). Figure 3 shows the signal-to-noise ratio for a fixed  $g_{a\gamma} = 10^{-10} \text{ GeV}^{-1}$  and time-independent Galactic radio emission. The signal-to-noise ratio is computed from Eqs. (26) and (27). When performing the integration over  $x$  in Eq. (26), we take the upper limit to be the virial radius of the Galaxy  $R_{\text{vir}} \simeq 221 \text{ kpc}$  [cf. Section 3.1], neglecting the small offset of the Earth from the Center of the DM halo. This is a good approximation since in Eq. (26) the contribution to  $S_\nu$  from the edge of the Galactic halo is expected to be insignificant. Also, when performing the angular integration in Eq. (26) we assume that the DM density is constant over each pixel of size 1.7 arcmin, which corresponds to the resolution of the Haslam map.

We compute the optical depth in Eq. (26) by setting the upper limit of the spatial integral at  $x = R_{\text{vir}}$  in Eq. (7). The optical depth at higher frequencies turns out to be quite small in all sky directions; therefore, its effect on the sky maps shown in Figure 3 is non-negligible only in the 50 MHz case. In order to reduce the computational time, we make an assumption that for a given line-of-sight distance, the optical depth is the same in any sky direction. This approximation results in conservatively estimating the flux of photons, especially from decays of axions close to the Earth. On the other hand, for axion

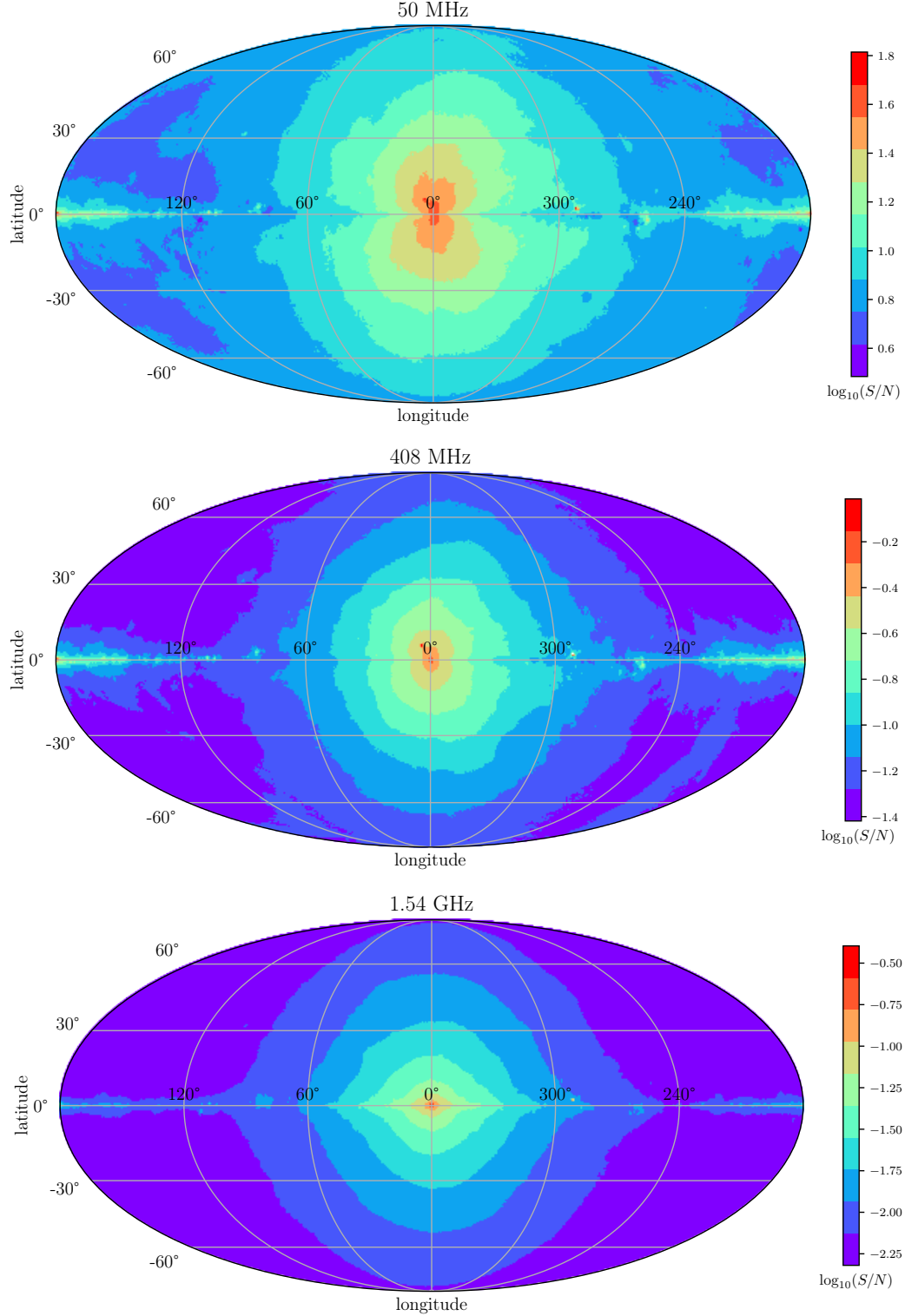


Figure 3: All-sky map (in Galactic coordinates) of the signal-to-noise ratio [cf. Eq. (26)] at 50 MHz (top), 408 MHz (middle), and 1.54 GHz (bottom). The axion-photon coupling is set to  $g_{a\gamma} = 10^{-10} \text{ GeV}^{-1}$  and we have used the NFW profile for DM density distribution.



decays in the close vicinity of the Galactic Center, Eq. (7) likely underestimates the optical depth. This is because the emission measure  $EM = \int dx n_e^2$  of radio photons from the Galactic Center that results from the electron number density in Eq. (11) is  $\mathcal{O}(10^2)$  pc cm<sup>-6</sup>, which is three orders of magnitude smaller than the estimate using the observed radio photon flux from Sgr A\* [87]. Nevertheless, we checked that this does not impact the flux from axion decays for the following reason. When observing the decay flux in the direction of the Galactic Center, the number of photons with momentum pointing away from the Galactic Center and towards the Earth at an intermediate point  $x$  would be  $e^{\tau(x)}$  times larger than that measured in the Haslam map,  $f_\gamma(x) = e^{\tau(x)} f_\gamma^\oplus$ . This is so because only photons unaffected by free-free absorption reach the Earth and are recorded in the Haslam map. As a result, the factor  $e^{\tau(x)}$  cancels out the factor  $e^{-\tau(x)}$  in Eq. (5), which takes into account the absorption of photons on their way from the axion decay point to the Earth. On the other hand, at the same point  $x$ , the number of photons traveling in the direction of the Galactic Center is  $e^{\tau(x)}$  times smaller compared to that observed at the Earth,  $\tilde{f}_\gamma^\oplus$ , coming from the Galactic Anti-center direction. Therefore, Eq. (5) can be approximated as

$$S_\nu \simeq \frac{\Gamma_a}{4\pi\Delta\nu} \int dx \int d\Omega \rho_a(x, \Omega) \left( f_\gamma(\Omega) + \tilde{f}_\gamma(\Omega) e^{-2\tau(\nu, x, \Omega)} \right). \quad (28)$$

From the Haslam map we deduce that the number of photons from the Galactic center  $f_\gamma(\Omega)$  is about 50 times larger than the number of photons from the Anti-Galactic Center  $\tilde{f}_\gamma(\Omega)$ . As a result,  $S_\nu$  from the Galactic Center does not depend strongly on the distribution of electrons in the Milky Way. This would not be necessarily the case when observing the photon flux from a direction where fewer background photons are observed compared to those from its antipodal direction. Nevertheless, we still expect the axion decay flux  $S_\nu$  to be largely independent of the electron number density, because for all other directions except near (within  $\sim 6^\circ$  of) the Galactic Center, the optical depth turns out to be negligible.

Let us stress that Eq. (28) is valid only if two conditions are satisfied: (i) the Galactic radio emission is time-independent, and (ii) the emissivity of photons everywhere along the line of sight is negligibly small, except near the Galactic Center. Therefore, it is fair to say that for diffuse emission, the Galactic Center is the dominant source. However, this approximation is clearly not valid for time-dependent point sources like SNRs; therefore, we will use the exact expression for the flux density (5) when estimating the gegenschein signal stimulated by the time-dependent radio flux from SNRs in Section 5.3.

## 5.2 Galactic Center versus Anti-center

From the all-sky maps we deduce that the Galactic Center is the most promising direction to look at for deriving the constraints in the  $(m_a, g_{a\gamma})$  plane from diffuse emission of radio photons due to stimulated axion decays. This is reasonable from Eq. (5) given the large density of axions around the Galactic Center, which produces a decay signal large enough to overcome the large background. Interestingly, the brightness in the direction of the Galactic Anti-center also stands out from the sky maps. This is so, because this direction benefits from the strong radio emission from the Galactic Center that stimulates axion decays and a much reduced foreground contamination. These two effects compensate for the reduced density of target DM axions at the Galactic Anti-center.

Before making a comparison of the Galactic Center and Anti-center with the point sources, we would like to compare the sensitivities derived using different radio telescopes. This is shown in Figure 4 for 100 hours of observation time in the Galactic Anti-center direction at the three different radio telescopes considered here, namely, FAST (green), SKA1 (red) and SKA2 (blue). Here we have used the NFW profile for the DM density distribution, but other profiles essentially give the same result, because away from the Galactic Center, the variation in the DM density among the different profiles is negligible. The shaded regions show the existing 95% C.L. exclusion limits (unless otherwise specified). The helioscope limit from CAST [45] is shown by the cyan shaded region. The green-shaded region shows the collective constraint (as compiled in Ref. [39]) from various haloscope experiments: ADMX [43], HAYSTAC [156, 157], ORGAN [158], UPLOAD [159], RBF [160, 161], UF [162], CAPP [163–167], CAST-CAPP [168],

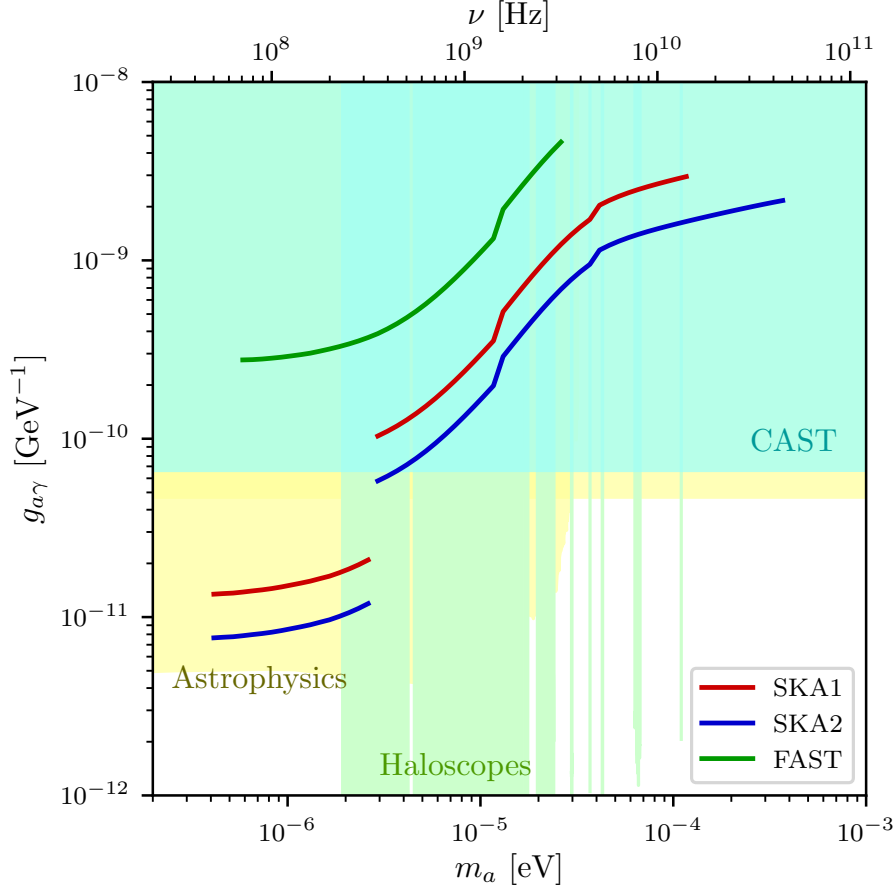


Figure 4: Comparing the sensitivity curves, corresponding to  $S/N > 1$  in Eq. (27), for stimulated axion decays in the direction of the Galactic Anti-center, derived using 100 hours of observation time at three different radio telescopes: FAST (green), SKA1 (red) and SKA2 (blue). The discontinuity at 350 MHz for SKA1 and SKA2 is due to the transition from SKA-low to SKA-mid [cf. Table 2]. The shaded regions show the current exclusion limits from CAST [45] (cyan), haloscopes [43] (light green) and astrophysics [47, 50] (yellow).

QUAX [169, 170], BASE [171], and TASEH [172]. The yellow-shaded region is the astrophysical constraint from the  $R_2$  parameter [47] (top right, just below CAST) and from pulsar data [50]. We find that the sensitivities derived are comparable to the current constraints, and moreover, can beat the CAST limit in the low-frequency regime. It should also be emphasized that the only constraint that beats our projected sensitivities is the pulsar limit [50] which is subject to astrophysical modeling uncertainties in the sourced axion spectrum, whereas our stimulated axion decay spectrum induced by diffuse emission is more robust against the astrophysical uncertainties, especially in the Galactic Anti-center direction. Since SKA2, not surprisingly, gives us the best sensitivity, we will show our following results only for SKA2.

In Figure 5, we compare the results in the direction of the Galactic Center (dark red) and Galactic Anti-center (blue). The solid (dotted) lines are obtained using NFW (Burkert) profile for the DM density distribution in the Galactic halo. Again we have used 100 hours of observation time at SKA2 and  $S/N > 1$  to derive the sensitivity curves. The Galactic radio emission is assumed to be constant in time. The shaded regions show the current exclusion, as in Figure 4.

The constraints from the Galactic Center can be compared to those reported in Ref. [58]. To reiterate the differences, in our analysis we include an amplification factor  $e^{\tau(x)}$  in the photon emissivity and we use the Haslam 408 MHz map to describe the Galactic radio emission, while Ref. [58] used the observed

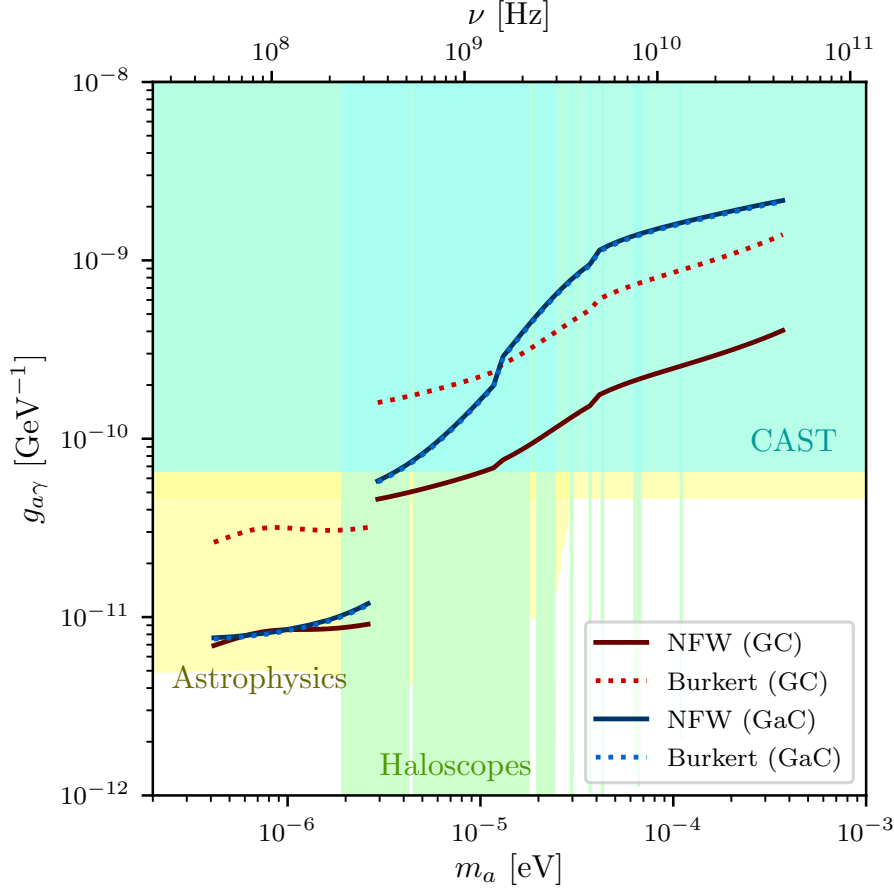


Figure 5: SKA2 sensitivity curves, corresponding to  $S/N > 1$  in Eq. (27), for stimulated axion decays in the direction of Galactic Center (dark red) and Galactic Anti-center (blue), obtained using NFW (solid) and Burkert (dotted) profiles for the DM density distribution in the Galactic halo. The shaded regions show the current exclusion limits from CAST [45] (cyan), haloscopes [43] (light green) and astrophysics [47, 50] (yellow).

photon energy density from the Galactic Center at  $\nu = 1.4$  GHz from Ref. [94]. In fact, their  $f_\gamma$  from the Galactic Center is 7-8 times larger than ours, but since it increases both the signal flux and the background by the same rate, the final result is similar to ours. In any case, the Galactic Anti-center result presented here is our main new point.

Possible uncertainties in our results could come from our limited knowledge of the electron distribution model, the axion DM distribution, and the spectrum of Galactic radio photon emission. The electron density enters the calculation of the free-free absorption of radio photons. This is an important effect, particularly at lower frequencies corresponding to  $m_a \lesssim 10^{-6}$  eV. The constraints from the Galactic Center are more susceptible to this absorption because of the large electron number density around the Galactic Center. The same goes for the density of DM axions in the central regions of the Galaxy, which can vary by orders of magnitude depending on whether one assumes a cuspy or a cored profile.

In contrast, the signal from the Galactic Anti-center is more robust, since there is less variation in the predictions for the mass density of DM axions in the outer parts of the Galaxy. Thus, the strength of these constraints will remain intact even assuming that the DM profile is cored, as we can see clearly in Figure 5. Moreover, the constraints from the Galactic Center might be weakened at low-frequencies, since, as mentioned before, we might be underestimating the emission measure EM in the direction of the Galactic Center [87]. In the frequency region that we consider, the number of photons is nearly proportional to the

brightness temperature:  $f_\gamma = (e^{E_\gamma/k_B T} - 1)^{-1} \simeq k_B T/E_\gamma$ . Thus, the signal-to-noise ratio is not sensitive to the frequency-dependence of the brightness temperature of the Galactic radio emission, as long as its contribution to the signal and the noise are dominant, as is the case at lower frequencies. Therefore, the uncertainty in the spectrum of Galactic radio photons will mainly affect the constraints at higher frequencies.

### 5.3 Point source sensitivity

Now we consider the four point sources listed in Table 1 and calculate the gegenschein signal from each of them. Figure 6 summarizes the constraints obtained by observing in the opposite directions to these SNRs. We first extract the contribution from Galactic synchrotron radiation from the Haslam map by subtracting the flux from supernova remnants estimated by extrapolating their observed flux with the spectral indices listed in Table 1. The image of an SNR is approximated by a circle with a diameter given in Table 1, and it is assumed to be unchanged during the evolution of the SNR. As before, we assume that the Galactic radio emission is time-independent. The time and frequency dependence of the radio emission from supernova remnants is estimated following the discussion in Section 3.4 with the spectral index for each SNR as listed in Table 1. Then, SKA2 sensitivities are obtained by letting  $S/N = 1$  in Eq. (27). The bands in Figure 6 capture the uncertainties associated with the SNR parameters, as discussed in Section 3.4. The dominant uncertainties come from the modeling of the flux and the MFA time. We have chosen the conservative model (ii)  $S_\nu \propto t^{-2(\gamma+1)/5}$  and  $t_{\text{MFA}} = 100$  years to draw the central curves and the bands are obtained by varying  $t_{\text{MFA}}$  between 30 and 300 years, as well as by using model (i)  $S_\nu \propto t^{-4\gamma/5}$ . The other SNR parameter uncertainties listed in Table 1 are also included, although their effects on the total uncertainty is small, except for the SNR age.

To reduce the computational time, two simplifications are made when estimating the results for W28, W50, and Vela. Firstly, free-free absorption is neglected in the frequency band measured by SKA-mid. We checked that this results in a negligible shift due to the small optical depth  $\tau \simeq 10^{-3}$ . On the other hand, the effect of free-free absorption is taken into account at the frequencies corresponding to SKA-low using the approximation  $\tau \simeq \tau(\nu, x = R_{\text{vir}}, \Omega = (l, b))$ . That is, we calculate  $\tau$  only in the opposite direction of each SNR and we neglect the directional-dependence of  $\tau$  inside the instantaneous field of view. This approximation is not valid for S147, because its anti-direction is close to the Galactic Center, and the optical depth is expected to depend strongly on the direction.

The strongest constraints at high frequencies are placed by S147 mainly because of the large axion mass density at the Galactic Center. The kink at  $m_a \simeq 15$  eV is caused by the abrupt change in the spectral index of S147 from  $\alpha = 0.3$  to 1.2 at  $\nu = 1.7$  GHz. A lower DM mass density at the Galactic Center would weaken the constraints from the Galactic Center and from S147. One mechanism that could remove mass from the inner region of the Galaxy is mass segregation due to dynamical friction. However, as discussed in Section 3.5, this effect turns out to be negligible. Comparing our results for Vela, W28 and W50 with those in Refs. [60, 61], we see that their results obtained from observations in the interferometric mode are better at high frequencies, whereas our results derived in the single-dish mode are better at low frequencies, where we can beat the CAST limit and be competitive with the pulsar limit.

Finally, in Figure 7, we summarize our results by collecting the sensitivities from all six sources considered in this study, namely, the gegenschein signals from the four SNRs shown in Figure 6, as well as the stimulated decay signals from the diffuse flux in the directions of Galactic Center and Anti-center shown in Figure 5. We find that at high frequencies ( $\nu > 350$  MHz), corresponding to  $m_a > 3.5 \times 10^{-6}$  eV, the Galactic Center gives the best sensitivity for the NFW profile. On the other hand, at low frequencies ( $\nu < 350$  MHz), the Galactic Anti-center gives better sensitivity than the Galactic Center, irrespective of the density profile. The point source sensitivities are better than the diffuse ones only for a cored profile like the Burkert.

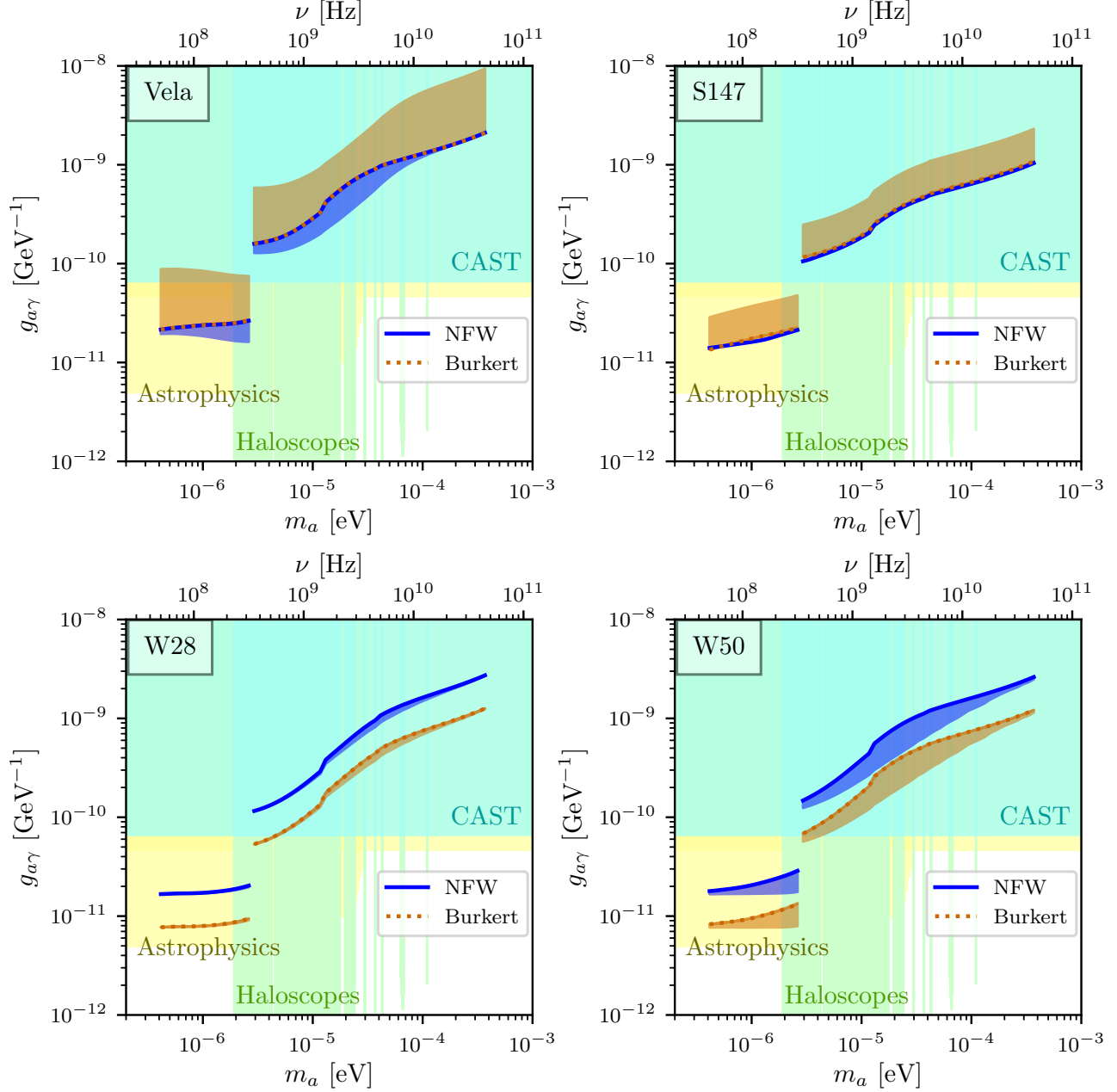


Figure 6: SKA2 sensitivity curves for the gegenschieen signal in the direction opposite to the SNR sources Vela (top left), S147 (top right), W28 (bottom left) and W50 (bottom right). The solid (dotted) curves correspond to the NFW (Burkert) profiles for the DM density distribution in the Galactic halo. The bands associated with each curve takes into account the SNR parameter uncertainties, as discussed in Section 3.4. The shaded regions show the current exclusion limits from CAST [45] (cyan), haloscopes [43] (light green) and astrophysics [47, 50] (yellow).

## 6 Conclusions

We have re-examined the constraints on the axion-photon coupling placed by the non-observation of radio photons from the stimulated decay of axion dark matter particles. In addition to the constant extragalactic radio emission and the CMB, we have included the Galactic radio emission with the spatial density empirically determined from the Haslam map at 408 MHz. With these diffuse sources of radio

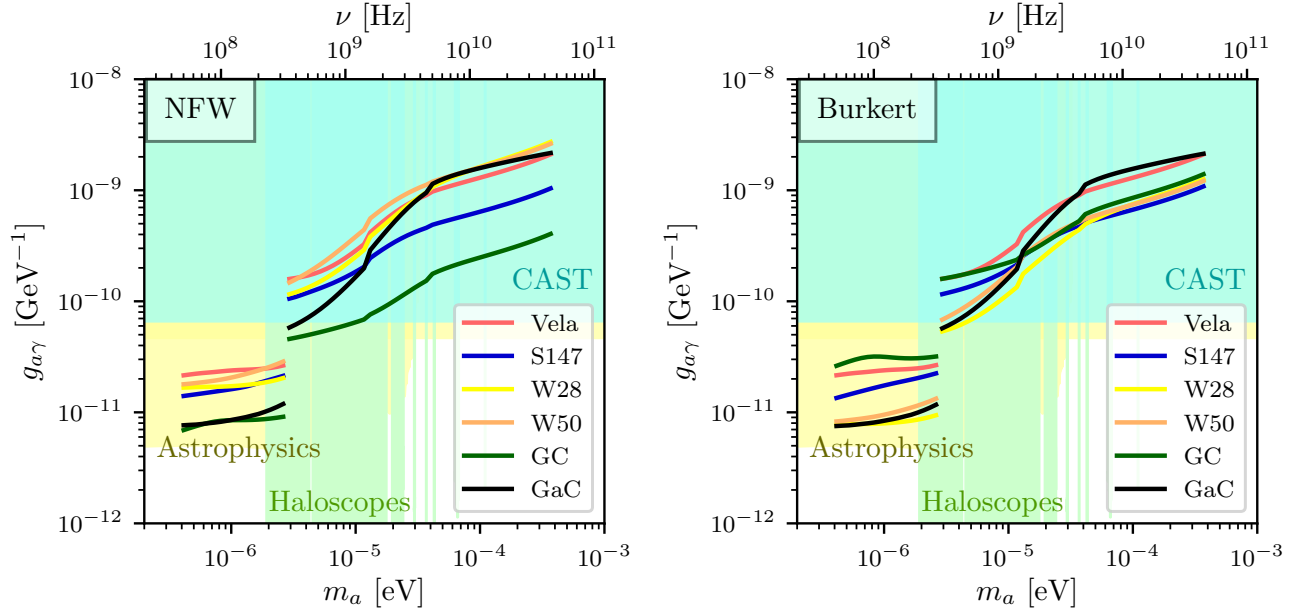


Figure 7: The summary plot comparing the SKA2 sensitivities for the stimulated axion decay signal for all the sources considered in this study, namely, the four SNRs, as well as the diffuse emission from the Galactic Center and Anti-center. The left (right) panel is assuming NFW (Burkert) profile for the DM density distribution in the Galactic halo. For the SNRs, we only show the central values of the sensitivities.

emission through the DM halo, we proceed to generate a full-sky map of the expected signal assuming 100 hours of observation each with the FAST and SKA telescopes. We also consider four selected supernova remnants that could potentially generate bright counterimages. Our final results are displayed in Figure 7 and show that, if the DM density follows a cuspy NFW profile, the Galactic Center provides the strongest constraints of order  $g_{a\gamma} \lesssim$  a few  $10^{-11} \text{ GeV}^{-1}$  for the frequencies observed by the SKA-low telescope.

Interestingly, our full-sky maps also suggest that the direction of the Galactic Anti-center can be used to place competitive constraints. Unlike the direct emission from the Galactic Center, the estimates from the Anti-center (which is technically the *gegenschein emission from the center*) do not depend on the highly uncertain DM density at the center of the halo, nor are impacted by a large optical depth. They are also arguably more robust than the limits from supernovæ that depend on assumptions about the radio emission during early stages in their evolution. Furthermore, if the Galactic DM halo is described by a cored profile, *the anti-center places not only the most robust but the most stringent constraints on the axion-photon coupling*.

**Note added:** During the final stages of our work, Refs. [173, 174] appeared. In [173], the authors update their previous analysis of the gegenschein signal and also consider the direct emission (“forwardschein”). Our conclusions largely agree where we overlap. Nevertheless, their focus is on point sources, while we compare the point source sensitivity to the diffuse emission sensitivities from the Galactic Center and Anti-center. In Ref. [174], the authors provide a detailed and general derivation of the effects, and focused on the case of Galactic pulsars as stimulating sources. The ensuing sensitivities are comparable to the SNR sensitivities shown here.



## Acknowledgments

We thank Sam Witte for useful discussion. This work was partly supported by the U.S. Department of Energy under grant No. DE-SC 0017987.

## A Stimulated decay of axions into photons

In this section we review the derivation of the stimulated axion decay in a photon bath, which was first discussed in Refs. [175–177] as a possible energy source in the central parts of dense axion clusters. The stimulated decay of axions is induced by the interaction term given in Eq. (1) and is greatly enhanced in astrophysical environments in the presence of an ambient radiation field and a large axion number density. We consider the general case where the photon distribution functions are not necessarily spherically symmetric (as assumed in Ref. [60]).

To find the evolution of the phase-space distribution function of photons  $f_\gamma(\mathbf{x}, \mathbf{p}, t) \equiv f_\lambda$ , we consider the process  $a(\mathbf{p}_a) \rightarrow \gamma(\mathbf{p}_1; \lambda) + \gamma(\mathbf{p}_2; \lambda)$  and its inverse  $\gamma(\mathbf{p}_1; \lambda) + \gamma(\mathbf{p}_2; \lambda) \rightarrow a(\mathbf{p}_a)$ , where  $\lambda = +, -$  denotes the helicity of photons. The conservation of angular momentum requires that the two photons emitted from the decay of a scalar or pseudo-scalar particle should have the same helicity, and the same applies to the two incoming photons in the inverse process. The evolution of the phase-space distribution function of the photon with momentum  $\mathbf{p}_1$  is given by the Boltzmann equation [60, 175–177]

$$\frac{d}{dt} f_{1\lambda} = \frac{1}{2E_1} \int \frac{d^3 p_a}{(2\pi)^3 2E_a} \int \frac{d^3 p_2}{(2\pi)^3 2E_2} |\mathcal{M}(f_a(1 + f_{1\lambda} + f_{2\lambda}) - f_{1\lambda} f_{2\lambda}) (2\pi)^4 \delta^{(4)}(p_a - p_1 - p_2)|, \quad (29)$$

where  $\mathcal{M} \equiv \mathcal{M}(a(\mathbf{p}_a) \rightarrow \gamma(\mathbf{p}_1; +) + \gamma(\mathbf{p}_2; +)) = \mathcal{M}(a(\mathbf{p}_a) \rightarrow \gamma(\mathbf{p}_1; -) + \gamma(\mathbf{p}_2; -))$  is the invariant decay amplitude determined by the Abelian chiral anomaly [178].

For all the environments that we consider the phase-space density of axions is much larger than that of photons,  $f_a \gg f_{i\lambda}$ , so we can neglect the last term  $\propto f_1 f_2$  corresponding to the inverse decay process in the collision integral. The first term  $\propto f_a$  describes the spontaneous decay of axions which, as shown in Eq. (3), has too large a lifetime to be experimentally detectable, and thus we also neglect it. The second and third terms,  $\propto f_a f_{i\lambda}$  correspond to the stimulated production of photons.

Assuming a parity symmetric photon field,  $f_{i+} = f_{i-} = \frac{1}{2} f_\gamma$ , we can sum over the helicities to obtain:

$$\begin{aligned} \frac{d}{dt} f_1 &= \frac{d}{dt} \sum_\lambda f_{1\lambda} = \frac{1}{2E_1} \int \frac{d^3 p_a}{(2\pi)^3 2E_a} \int \frac{d^3 p_2}{(2\pi)^3 2E_2} (2\pi)^4 \delta^{(4)}(p_a - p_1 - p_2) \\ &\quad \times f_a (f_1 + f_2) \frac{1}{2} \sum_\lambda |\mathcal{M}(a(\mathbf{p}_a) \rightarrow \gamma(\mathbf{p}_1; \lambda) + \gamma(\mathbf{p}_2; \lambda))|^2. \end{aligned} \quad (30)$$

To leading order we can take the axion dark matter to be cold, neglecting the small velocity dispersion in the Galaxy  $\sigma_v \approx 5 \times 10^{-4}$  [66]. With this assumption, the axion distribution function is given by  $f_a = (2\pi)^3 n_a(\mathbf{x}) \delta^{(3)}(\mathbf{p}_a)$ , where  $n_a(\mathbf{x})$  is the axion number density. Thus, the photon production rate is

$$\begin{aligned} \frac{d}{dt} f_1 &= \frac{\rho_a(\mathbf{x})}{4m_a^2 E_1} \int \frac{d^3 p_2}{(2\pi)^3 2E_2} (f_1(\mathbf{x}, \mathbf{p}_1, t) + f_2(\mathbf{x}, \mathbf{p}_2, t)) (2\pi)^4 \delta(m_a - E_1 - E_2) \delta^{(3)}(\mathbf{p}_1 + \mathbf{p}_2) \\ &\quad \times \frac{1}{2} \sum_\lambda |\mathcal{M}(a(\mathbf{0}) \rightarrow \gamma(\mathbf{p}_1; \lambda) + \gamma(\mathbf{p}_2; \lambda))|^2, \end{aligned} \quad (31)$$

where  $\rho_a(\mathbf{x}) = m_a n_a(\mathbf{x})$ . Integrating over  $\mathbf{p}_2$  and identifying  $f_i$  with  $f_\gamma$  (traveling either forward or backward along the line of sight), we get

$$\frac{d}{dt} f_\gamma(\mathbf{x}, \mathbf{p}, t) = \frac{\pi \rho_a(\mathbf{x})}{4m_a^2 E_\gamma^2} (f_\gamma(\mathbf{x}, \mathbf{p}, t) + f_\gamma(\mathbf{x}, -\mathbf{p}, t)) \delta(m_a - 2E_\gamma) \frac{1}{2} \sum_\lambda |\mathcal{M}(a(\mathbf{0}) \rightarrow \gamma(\mathbf{p}; \lambda) + \gamma(-\mathbf{p}; \lambda))|^2. \quad (32)$$

We see that the energy  $E$  of the two outgoing photons is equal to  $m_a/2$  due to the conservation of energy. Substituting the expression of the spontaneous decay rate in the rest frame of an axion,

$$\Gamma_a = \tau_a^{-1} = \frac{m_a^3 g_{a\gamma}^2}{64\pi} = \frac{1}{8\pi} \frac{1}{2m_a} \frac{1}{2} \sum_{\lambda} |\mathcal{M}(a(\mathbf{0}) \rightarrow \gamma(\mathbf{p}; \lambda) + \gamma(-\mathbf{p}; \lambda))|^2, \quad (33)$$

into Eq. (32), we finally obtain the time derivative of the photon distribution function as

$$\frac{d}{dt} f_{\gamma}(\mathbf{x}, \mathbf{p}, t) = \frac{\pi^2 \Gamma_a \rho_a(\mathbf{x})}{E_{\gamma}^3} (f_{\gamma}(\mathbf{x}, \mathbf{p}, t) + f_{\gamma}(\mathbf{x}, -\mathbf{p}, t)) \delta(E_{\gamma} - m_a/2). \quad (34)$$

This expression implies that we will observe photons from decays of axions stimulated by the photons traveling either towards the Earth (the first term) or away from the Earth (the second term) and both having energy equal to half of the axion mass. Although we assumed that the axion DM is at rest in the Galaxy, this conclusion is true in general: two photons with the same energy are emitted back-to-back in the rest frame of the axion.

Integrating the photon distribution function obtained from Eq. (34) over the phase space solid angle, we get the phase space density  $S_{\nu} = 2\nu^3 \int d\Omega f_{\gamma}$ , where  $\nu = E_{\gamma}/2\pi = m_a/4\pi$  is the frequency of the photon. Integrating the phase space density over the distance along the line of sight, and averaging over the photon bandwidth, we obtain the flux density given in Eq. (5).

## References

- [1] R. D. Peccei and H. R. Quinn, “CP Conservation in the Presence of Instantons,” [Phys. Rev. Lett. \*\*38\*\* \(1977\) 1440–1443](#).
- [2] S. Weinberg, “A New Light Boson?,” [Phys. Rev. Lett. \*\*40\*\* \(1978\) 223–226](#).
- [3] F. Wilczek, “Problem of Strong  $P$  and  $T$  Invariance in the Presence of Instantons,” [Phys. Rev. Lett. \*\*40\*\* \(1978\) 279–282](#).
- [4] J. Preskill, M. B. Wise, and F. Wilczek, “Cosmology of the Invisible Axion,” [Phys. Lett. B \*\*120\*\* \(1983\) 127–132](#).
- [5] L. F. Abbott and P. Sikivie, “A Cosmological Bound on the Invisible Axion,” [Phys. Lett. B \*\*120\*\* \(1983\) 133–136](#).
- [6] M. Dine and W. Fischler, “The Not So Harmless Axion,” [Phys. Lett. B \*\*120\*\* \(1983\) 137–141](#).
- [7] J. Ipser and P. Sikivie, “Are Galactic Halos Made of Axions?,” [Phys. Rev. Lett. \*\*50\*\* \(1983\) 925](#).
- [8] P. Svrcek and E. Witten, “Axions In String Theory,” [JHEP \*\*06\*\* \(2006\) 051](#), [[hep-th/0605206](#)].
- [9] A. Arvanitaki, S. Dimopoulos, S. Dubovsky, N. Kaloper, and J. March-Russell, “String Axiverse,” [Phys. Rev. D \*\*81\*\* \(2010\) 123530](#), [[0905.4720](#)].
- [10] L. Di Luzio, M. Giannotti, E. Nardi, and L. Visinelli, “The landscape of QCD axion models,” [Phys. Rept. \*\*870\*\* \(2020\) 1–117](#), [[2003.01100](#)].
- [11] I. G. Irastorza and J. Redondo, “New experimental approaches in the search for axion-like particles,” [Prog. Part. Nucl. Phys. \*\*102\*\* \(2018\) 89–159](#), [[1801.08127](#)].
- [12] K. Choi, S. H. Im, and C. Sub Shin, “Recent Progress in the Physics of Axions and Axion-Like Particles,” [Ann. Rev. Nucl. Part. Sci. \*\*71\*\* \(2021\) 225–252](#), [[2012.05029](#)].

- [13] J. E. Kim, “Weak Interaction Singlet and Strong CP Invariance,” [Phys. Rev. Lett.](#) **43** (1979) 103.
- [14] M. A. Shifman, A. I. Vainshtein, and V. I. Zakharov, “Can Confinement Ensure Natural CP Invariance of Strong Interactions?,” [Nucl. Phys. B](#) **166** (1980) 493–506.
- [15] A. R. Zhitnitsky, “On Possible Suppression of the Axion Hadron Interactions. (In Russian),” [Sov. J. Nucl. Phys.](#) **31** (1980) 260.
- [16] M. Dine, W. Fischler, and M. Srednicki, “A Simple Solution to the Strong CP Problem with a Harmless Axion,” [Phys. Lett. B](#) **104** (1981) 199–202.
- [17] M. Gorghetto and G. Villadoro, “Topological Susceptibility and QCD Axion Mass: QED and NNLO corrections,” [JHEP](#) **03** (2019) 033, [[1812.01008](#)].
- [18] P. Sikivie, “Axion Cosmology,” [Lect. Notes Phys.](#) **741** (2008) 19–50, [[astro-ph/0610440](#)].
- [19] D. J. E. Marsh, “Axion Cosmology,” [Phys. Rept.](#) **643** (2016) 1–79, [[1510.07633](#)].
- [20] M. S. Turner, “Thermal Production of Not SO Invisible Axions in the Early Universe,” [Phys. Rev. Lett.](#) **59** (1987) 2489. [Erratum: [Phys.Rev.Lett.](#) 60, 1101 (1988)].
- [21] L. Covi, H.-B. Kim, J. E. Kim, and L. Roszkowski, “Axinos as dark matter,” [JHEP](#) **05** (2001) 033, [[hep-ph/0101009](#)].
- [22] A. Brandenburg and F. D. Steffen, “Axino dark matter from thermal production,” [JCAP](#) **08** (2004) 008, [[hep-ph/0405158](#)].
- [23] A. Salvio, A. Strumia, and W. Xue, “Thermal axion production,” [JCAP](#) **01** (2014) 011, [[1310.6982](#)].
- [24] R. L. Davis, “Cosmic Axions from Cosmic Strings,” [Phys. Lett. B](#) **180** (1986) 225–230.
- [25] D. Harari and P. Sikivie, “On the Evolution of Global Strings in the Early Universe,” [Phys. Lett. B](#) **195** (1987) 361–365.
- [26] D. H. Lyth, “Estimates of the cosmological axion density,” [Phys. Lett. B](#) **275** (1992) 279–283.
- [27] T. Hiramatsu, M. Kawasaki, K. Saikawa, and T. Sekiguchi, “Production of dark matter axions from collapse of string-wall systems,” [Phys. Rev. D](#) **85** (2012) 105020, [[1202.5851](#)]. [Erratum: [Phys.Rev.D](#) 86, 089902 (2012)].
- [28] M. Buschmann, J. W. Foster, A. Hook, A. Peterson, D. E. Willcox, W. Zhang, and B. R. Safdi, “Dark matter from axion strings with adaptive mesh refinement,” [Nature Commun.](#) **13** no. 1, (2022) 1049, [[2108.05368](#)].
- [29] B. S. Acharya, K. Bobkov, and P. Kumar, “An M Theory Solution to the Strong CP Problem and Constraints on the Axiverse,” [JHEP](#) **11** (2010) 105, [[1004.5138](#)].
- [30] M. Cicoli, J. P. Conlon, and F. Quevedo, “Dark radiation in LARGE volume models,” [Phys. Rev. D](#) **87** no. 4, (2013) 043520, [[1208.3562](#)].
- [31] T. Higaki and F. Takahashi, “Dark Radiation and Dark Matter in Large Volume Compactifications,” [JHEP](#) **11** (2012) 125, [[1208.3563](#)].
- [32] J. P. Conlon and M. C. D. Marsh, “The Cosmophenomenology of Axionic Dark Radiation,” [JHEP](#) **10** (2013) 214, [[1304.1804](#)].

- [33] T. Higaki, K. Nakayama, and F. Takahashi, “Moduli-Induced Axion Problem,” [JHEP](#) **07** (2013) 005, [[1304.7987](#)].
- [34] H. Baer, V. Barger, and R. W. Deal, “On dark radiation from string moduli decay to ALPs,” [JHEAp](#) **34** (2022) 40–48, [[2204.01130](#)].
- [35] M. Cicoli, J. P. Conlon, A. Maharana, S. Parameswaran, F. Quevedo, and I. Zavala, “String Cosmology: from the Early Universe to Today,” [[2303.04819](#)].
- [36] F. Schiavone, D. Montanino, A. Mirizzi, and F. Capozzi, “Axion-like particles from primordial black holes shining through the Universe,” [JCAP](#) **08** (2021) 063, [[2107.03420](#)].
- [37] K. Mazde and L. Visinelli, “The interplay between the dark matter axion and primordial black holes,” [JCAP](#) **01** (2023) 021, [[2209.14307](#)].
- [38] T. Li and R.-J. Zhang, “Axionlike particles from primordial black hole evaporation and their detection in neutrino experiments,” [Phys. Rev. D](#) **106** no. 9, (2022) 095034, [[2208.02696](#)].
- [39] C. O’Hare, “cajohare/axionlimits: Axionlimits.” <https://cajohare.github.io/AxionLimits/>, July, 2020.
- [40] P. Sikivie, “Experimental Tests of the Invisible Axion,” [Phys. Rev. Lett.](#) **51** (1983) 1415–1417. [Erratum: [Phys.Rev.Lett.](#) 52, 695 (1984)].
- [41] **ADMX** Collaboration, N. Du et al., “A Search for Invisible Axion Dark Matter with the Axion Dark Matter Experiment,” [Phys. Rev. Lett.](#) **120** no. 15, (2018) 151301, [[1804.05750](#)].
- [42] **ADMX** Collaboration, T. Braine et al., “Extended Search for the Invisible Axion with the Axion Dark Matter Experiment,” [Phys. Rev. Lett.](#) **124** no. 10, (2020) 101303, [[1910.08638](#)].
- [43] **ADMX** Collaboration, C. Bartram et al., “Search for Invisible Axion Dark Matter in the 3.3–4.2  $\mu\text{eV}$  Mass Range,” [Phys. Rev. Lett.](#) **127** no. 26, (2021) 261803, [[2110.06096](#)].
- [44] **ADMX** Collaboration, C. Bartram et al., “Dark matter axion search using a Josephson Traveling wave parametric amplifier,” [Rev. Sci. Instrum.](#) **94** no. 4, (2023) 044703, [[2110.10262](#)].
- [45] **CAST** Collaboration, V. Anastassopoulos et al., “New CAST Limit on the Axion-Photon Interaction,” [Nature Phys.](#) **13** (2017) 584–590, [[1705.02290](#)].
- [46] A. Ayala, I. Domínguez, M. Giannotti, A. Mirizzi, and O. Straniero, “Revisiting the bound on axion-photon coupling from Globular Clusters,” [Phys. Rev. Lett.](#) **113** no. 19, (2014) 191302, [[1406.6053](#)].
- [47] M. J. Dolan, F. J. Hiskens, and R. R. Volkas, “Advancing globular cluster constraints on the axion-photon coupling,” [JCAP](#) **10** (2022) 096, [[2207.03102](#)].
- [48] J. W. Foster, S. J. Witte, M. Lawson, T. Linden, V. Gajjar, C. Weniger, and B. R. Safdi, “Extraterrestrial Axion Search with the Breakthrough Listen Galactic Center Survey,” [Phys. Rev. Lett.](#) **129** no. 25, (2022) 251102, [[2202.08274](#)].
- [49] A. Prabhu, “Axion production in pulsar magnetosphere gaps,” [Phys. Rev. D](#) **104** no. 5, (2021) 055038, [[2104.14569](#)].
- [50] D. Noordhuis, A. Prabhu, S. J. Witte, A. Y. Chen, F. Cruz, and C. Weniger, “Novel Constraints on Axions Produced in Pulsar Polar-Cap Cascades,” [Phys. Rev. Lett.](#) **131** no. 11, (2023) 111004, [[2209.09917](#)].

- [51] M. Drewes et al., “A White Paper on keV Sterile Neutrino Dark Matter,” [JCAP](#) **01** (2017) 025, [[1602.04816](#)].
- [52] A. Ibarra, D. Tran, and C. Weniger, “Indirect Searches for Decaying Dark Matter,” [Int. J. Mod. Phys. A](#) **28** (2013) 1330040, [[1307.6434](#)].
- [53] A. Arza and P. Sikivie, “Production and detection of an axion dark matter echo,” [Phys. Rev. Lett.](#) **123** no. 13, (2019) 131804, [[1902.00114](#)].
- [54] A. Arza and E. Todarello, “Axion dark matter echo: A detailed analysis,” [Phys. Rev. D](#) **105** no. 2, (2022) 023023, [[2108.00195](#)].
- [55] Y. Gong, X. Liu, L. Wu, Q. Yang, and B. Zhu, “Detecting Ultra-light Dark Matter with Stimulated Annihilation,” [[2308.08477](#)].
- [56] A. Arza, Q. Guo, L. Wu, Q. Yang, X. Yang, Q. Yuan, and B. Zhu, “Listening for the Axion Echo with the 21 CentiMeter Array,” [[2309.06857](#)].
- [57] A. Caputo, C. P. Garay, and S. J. Witte, “Looking for Axion Dark Matter in Dwarf Spheroidals,” [Phys. Rev. D](#) **98** no. 8, (2018) 083024, [[1805.08780](#)]. [Erratum: [Phys.Rev.D](#) 99, 089901 (2019)].
- [58] A. Caputo, M. Regis, M. Taoso, and S. J. Witte, “Detecting the Stimulated Decay of Axions at RadioFrequencies,” [JCAP](#) **03** (2019) 027, [[1811.08436](#)].
- [59] O. Ghosh, J. Salvado, and J. Miralda-Escudé, “Axion Gegenschein: Probing Back-scattering of Astrophysical Radio Sources Induced by Dark Matter,” [[2008.02729](#)].
- [60] M. A. Buen-Abad, J. Fan, and C. Sun, “Axion echoes from the supernova graveyard,” [Phys. Rev. D](#) **105** no. 7, (2022) 075006, [[2110.13916](#)].
- [61] Y. Sun, K. Schutz, A. Nambrath, C. Leung, and K. Masui, “Axion dark matter-induced echo of supernova remnants,” [Phys. Rev. D](#) **105** no. 6, (2022) 063007, [[2110.13920](#)].
- [62] R. Nan, D. Li, C. Jin, Q. Wang, L. Zhu, W. Zhu, H. Zhang, Y. Yue, and L. Qian, “The Five-Hundred-Meter Aperture Spherical Radio Telescope (FAST) Project,” [Int. J. Mod. Phys. D](#) **20** (2011) 989–1024, [[1105.3794](#)].
- [63] R. Braun, A. Bonaldi, T. Bourke, E. Keane, and J. Wagg, “Anticipated Performance of the Square Kilometre Array – Phase 1 (SKA1),” [[1912.12699](#)].
- [64] S. F. Singer, “Cosmic radio waves,” [Science](#) **133** (1961) 1248–1249. Translated by R. B. Rodman and C. M. Varsavsky.
- [65] P. C. Gregory and E. R. Seaquist, “The nature of cygnus x-3 radio outbursts from an analysis of radiofrequency spectra,” [Astrophys. J.](#) **194** (1974) 715–723.
- [66] K. Freese, M. Lisanti, and C. Savage, “Colloquium: Annual modulation of dark matter,” [Rev. Mod. Phys.](#) **85** (2013) 1561–1581, [[1209.3339](#)].
- [67] P. J. McMillan, “Mass models of the milky way,” [Mon. Not. Roy. Astron. Soc.](#) **414** no. 3, (2011) 2446–2457, [[1102.4340](#)].
- [68] P. J. McMillan, “The mass distribution and gravitational potential of the milky way,” [Mon. Not. Roy. Astron. Soc.](#) **465** no. 1, (2016) 76–94, [[1608.00971](#)].
- [69] J. Binney and S. Tremaine, [Galactic dynamics](#), vol. 13. Princeton university press, 2011.

- [70] J. F. Navarro, C. S. Frenk, and S. D. M. White, “A Universal density profile from hierarchical clustering,” [\*Astrophys. J.\* \*\*490\*\* \(1997\) 493–508](#), [[astro-ph/9611107](#)].
- [71] T. Callingham, M. Cautun, A. J. Deason, C. S. Frenk, W. Wang, F. A. Gómez, R. J. J. Grand, F. Marinacci, and R. Pakmor, “The mass of the Milky Way from satellite dynamics,” [\*Mon. Not. Roy. Astron. Soc.\* \*\*484\*\* \(8, 2018\) 5453](#), [[1808.10456](#)].
- [72] L. H. Cooke et al., “Cuspy dark matter density profiles in massive dwarf galaxies,” [\*Mon. Not. Roy. Astron. Soc.\* \*\*512\*\* no. 1, \(2022\) 1012–1031](#), [[2203.00694](#)].
- [73] R. A. Flores and J. R. Primack, “Observational and theoretical constraints on singular dark matter halos,” [\*Astrophys. J. Lett.\* \*\*427\*\* \(1994\) L1–4](#), [[astro-ph/9402004](#)].
- [74] B. Moore, “Evidence against dissipationless dark matter from observations of galaxy haloes,” [\*Nature\* \*\*370\*\* \(1994\) 629](#).
- [75] B. Moore, T. R. Quinn, F. Governato, J. Stadel, and G. Lake, “Cold collapse and the core catastrophe,” [\*Mon. Not. Roy. Astron. Soc.\* \*\*310\*\* \(1999\) 1147–1152](#), [[astro-ph/9903164](#)].
- [76] A. V. Macció, A. A. Dutton, and F. C. van den Bosch, “Concentration, Spin and Shape of Dark Matter Haloes as a Function of the Cosmological Model: WMAP1, WMAP3 and WMAP5 results,” [\*Mon. Not. Roy. Astron. Soc.\* \*\*391\*\* \(2008\) 1940–1954](#), [[0805.1926](#)].
- [77] M. G. Walker and J. Penarrubia, “A Method for Measuring (Slopes of) the Mass Profiles of Dwarf Spheroidal Galaxies,” [\*Astrophys. J.\* \*\*742\*\* \(2011\) 20](#), [[1108.2404](#)].
- [78] N. C. Amorisco, A. Agnello, and N. W. Evans, “The core size of the Fornax dwarf Spheroidal,” [\*Mon. Not. Roy. Astron. Soc.\* \*\*429\*\* \(2013\) L89–L93](#), [[1210.3157](#)].
- [79] T. K. Chan, D. Kereš, J. Oñorbe, P. F. Hopkins, A. L. Muratov, C. A. Faucher-Giguère, and E. Quataert, “The impact of baryonic physics on the structure of dark matter haloes: the view from the FIRE cosmological simulations,” [\*Mon. Not. Roy. Astron. Soc.\* \*\*454\*\* no. 3, \(2015\) 2981–3001](#), [[1507.02282](#)].
- [80] A. Burkert, “The Structure of dark matter halos in dwarf galaxies,” [\*Astrophys. J. Lett.\* \*\*447\*\* \(1995\) L25](#), [[astro-ph/9504041](#)].
- [81] M. Cirelli, G. Corcella, A. Hektor, G. Hutsi, M. Kadastik, P. Panci, M. Raidal, F. Sala, and A. Strumia, “PPPC 4 DM ID: A Poor Particle Physicist Cookbook for Dark Matter Indirect Detection,” [\*JCAP\* \*\*03\*\* \(2011\) 051](#), [[1012.4515](#)]. [Erratum: *JCAP* 10, E01 (2012)].
- [82] D. H. F. M. Schnitzeler, “Modelling the Galactic distribution of free electrons,” [\*Mon. Not. Roy. Astron. Soc.\* \*\*427\*\* \(2012\) 664–678](#), [[1208.3045](#)].
- [83] G. C. Gomez, R. A. Benjamin, D. P. Cox, and P. Donald, “A re-examination of the distribution of galactic free electrons,” [\*Astron. J.\* \*\*122\*\* \(2001\) 908](#), [[astro-ph/0105416](#)].
- [84] J. H. Taylor and J. M. Cordes, “Pulsar Distances and the Galactic Distribution of Free Electrons,” [\*Astrophys. J.\* \*\*411\*\* \(1993\) 674](#).
- [85] E. M. Berkhuijsen and P. Mueller, “Densities and filling factors of the DIG in the Solar neighbourhood,” [\*Astron. Astrophys.\* \*\*490\*\* \(2008\) 179](#), [[0807.3686](#)].
- [86] B. M. Gaensler, G. J. Madsen, S. Chatterjee, and S. A. Mao, “The Vertical Structure of Warm Ionised Gas in the Milky Way,” [\*Publ. Astron. Soc. Austral.\* \*\*25\*\* \(2008\) 184–200](#), [[0808.2550](#)].



- [87] A. Pedlar, K. R. Anantharamaiah, R. D. Ekers, W. M. Goss, J. H. van Gorkom, U. J. Schwarz, and J.-H. Zhao, “Radio Studies of the Galactic Center. I. The Sagittarius A Complex,” [\*Astrophys. J.\* \*\*342\*\* \(1989\) 769](#).
- [88] C. Quireza, R. T. Rood, T. M. Bania, D. S. Balser, and W. J. Maciel, “The Electron Temperature Gradient in the Galactic Disk,” [\*Astrophys. J.\* \*\*653\*\* \(2006\) 1226–1240](#), [[astro-ph/0609006](#)].
- [89] D. J. Fixsen, “The Temperature of the Cosmic Microwave Background,” [\*Astrophys. J.\* \*\*707\*\* \(2009\) 916–920](#), [[0911.1955](#)].
- [90] N. Fornengo, R. A. Lineros, M. Regis, and M. Taoso, “The isotropic radio background revisited,” [\*JCAP\* \*\*04\*\* \(2014\) 008](#), [[1402.2218](#)].
- [91] C. G. T. Haslam, U. Klein, C. J. Salter, H. Stoffel, W. E. Wilson, M. N. Cleary, D. J. Cooke, and P. Thomasson, “A 408 MHz all-sky continuum survey. I - Observations at southern declinations and for the North Polar region,” [\*Astron. Astrophys.\* \*\*100\*\* \(1981\) 209–219](#).
- [92] C. G. T. Haslam, C. J. Salter, H. Stoffel, and W. E. Wilson, “A 408-MHz All-Sky Continuum Survey. II. The Atlas of Contour Maps,” [\*Astron. astrophys., Suppl. Ser.\* \*\*47\*\* \(1982\) 1](#).
- [93] A. E. Guzmán, J. May, H. Alvarez, and K. Maeda, “All-sky Galactic radiation at 45 MHz and spectral index between 45 and 408 MHz,” [\*Astron. Astrophys.\* \*\*525\*\* \(2011\) A138](#), [[1011.4298](#)].
- [94] F. Yusef-Zadeh *et al.*, “Interacting Cosmic Rays with Molecular Clouds: A Bremsstrahlung Origin of Diffuse High Energy Emission from the Inner 2deg by 1deg of the Galactic Center,” [\*Astrophys. J.\* \*\*762\*\* \(2013\) 33](#), [[1206.6882](#)].
- [95] J. Vink, “Supernova remnants: the X-ray perspective,” [\*Astron. Astrophys. Rev.\* \*\*20\*\* \(2012\) 49](#), [[1112.0576](#)].
- [96] G. Dubner and E. Giacani, “Radio emission from Supernova Remnants,” [\*Astron. Astrophys. Rev.\* \*\*23\*\* no. 1, \(2015\) 3](#), [[1508.07294](#)].
- [97] J. Vink, [\*Physics and Evolution of Supernova Remnants\*](#). Springer, 2020.
- [98] L. Woltjer, “Supernova remnants,” [\*Ann. Rev. Astron. Astrophys.\* \*\*10\*\* \(1972\) 129–158](#).
- [99] B. T. Draine, [\*Physics of the interstellar and intergalactic medium\*](#), vol. 19. Princeton University Press, 2010.
- [100] J. K. Truelove and C. F. McKee, “Evolution of Nonradiative Supernova Remnants,” [\*Astrophys. J. Suppl. Ser.\* \*\*120\*\* no. 2, \(1999\) 299–326](#).
- [101] I. S. Shklovskii, “Secular Variation of the Flux and Intensity of Radio Emission from Discrete Sources,” [\*Sov. Astron.\* \*\*4\*\* \(1960\) 243](#).
- [102] D. Urošević, M. Z. Pavlović, and B. Arbutina, “On the foundation of equipartition in supernova remnants,” [\*Astrophys. J.\* \*\*855\*\* no. 1, \(2018\) 59](#), [[1801.10422](#)].
- [103] K. Rohlfs and T. L. Wilson, [\*Tools of radio astronomy\*](#). Springer Science & Business Media, 2013.
- [104] T. Inoue, R. Yamazaki, and S.-i. Inutsuka, “Turbulence and Magnetic Field Amplification in Supernova Remnants: Interactions Between a Strong Shock Wave and Multiphase Interstellar Medium,” [\*Astrophys. J.\* \*\*695\*\* no. 2, \(2009\) 825–833](#), [[0901.0486](#)].

- [105] M. Z. Pavlović, D. Urošević, B. Arbutina, S. Orlando, N. Maxted, and M. D. Filipović, “Radio Evolution of Supernova Remnants Including Nonlinear Particle Acceleration: Insights from Hydrodynamic Simulations,” [\*Astrophys. J.\* \*\*852\*\* no. 2, \(2018\) 84, \[1711.06013\]](#).
- [106] D. A. Green, “A revised catalogue of 294 Galactic supernova remnants,” [\*J. Astrophys. Astron.\* \*\*40\*\* no. 4, \(2019\) 36, \[1907.02638\]](#).
- [107] D. A. Green, “A catalogue of galactic supernova remnants (2022 december version).” <https://www.mrao.cam.ac.uk/surveys/snrs/>, 2022. Cavendish Laboratory, Cambridge, United Kingdom.
- [108] G. Ferrand and S. Safi-Harb, “A Census of High-Energy Observations of Galactic Supernova Remnants,” [\*Adv. Space Res.\* \*\*49\*\* \(2012\) 1313–1319, \[1202.0245\]](#).
- [109] G. Ferrand and S. Safi-Harb, “SNRcat - High Energy Observations of Galactic Supernova Remnants.” <http://snrcat.physics.umanitoba.ca>.
- [110] W. Reich, X. Zhang, and E. Fürst, “35 cm observations of a sample of large supernova remnants,” [\*Astron. Astrophys.\* \*\*408\*\* \(2003\) 961–969](#).
- [111] C. J. Hogan and M. J. Rees, “Axion Miniclusters,” [\*Phys. Lett. B\* \*\*205\*\* \(1988\) 228–230](#).
- [112] E. W. Kolb and I. I. Tkachev, “Axion miniclusters and Bose stars,” [\*Phys. Rev. Lett.\* \*\*71\*\* \(1993\) 3051–3054, \[hep-ph/9303313\]](#).
- [113] E. W. Kolb and I. I. Tkachev, “Nonlinear axion dynamics and formation of cosmological pseudosolitons,” [\*Phys. Rev. D\* \*\*49\*\* \(1994\) 5040–5051, \[astro-ph/9311037\]](#).
- [114] A. Vaquero, J. Redondo, and J. Stadler, “Early seeds of axion miniclusters,” [\*JCAP\* \*\*04\*\* \(2019\) 012, \[1809.09241\]](#).
- [115] M. Buschmann, J. W. Foster, and B. R. Safdi, “Early-Universe Simulations of the Cosmological Axion,” [\*Phys. Rev. Lett.\* \*\*124\*\* no. 16, \(2020\) 161103, \[1906.00967\]](#).
- [116] B. Eggemeier, J. Redondo, K. Dolag, J. C. Niemeyer, and A. Vaquero, “First Simulations of Axion Minicluster Halos,” [\*Phys. Rev. Lett.\* \*\*125\*\* no. 4, \(2020\) 041301, \[1911.09417\]](#).
- [117] D. Ellis, D. J. E. Marsh, and C. Behrens, “Axion Miniclusters Made Easy,” [\*Phys. Rev. D\* \*\*103\*\* no. 8, \(2021\) 083525, \[2006.08637\]](#).
- [118] H. Xiao, I. Williams, and M. McQuinn, “Simulations of axion minihalos,” [\*Phys. Rev. D\* \*\*104\*\* no. 2, \(2021\) 023515, \[2101.04177\]](#).
- [119] D. Ellis, D. J. E. Marsh, B. Eggemeier, J. Niemeyer, J. Redondo, and K. Dolag, “Structure of axion miniclusters,” [\*Phys. Rev. D\* \*\*106\*\* no. 10, \(2022\) 103514, \[2204.13187\]](#).
- [120] V. Dandoy, T. Schwetz, and E. Todarello, “A self-consistent wave description of axion miniclusters and their survival in the galaxy,” [\*JCAP\* \*\*09\*\* \(2022\) 081, \[2206.04619\]](#).
- [121] G. Pierobon, J. Redondo, K. Saikawa, A. Vaquero, and G. D. Moore, “Miniclusters from axion string simulations,” [\[2307.09941\]](#).
- [122] D. J. Kaup, “Klein-Gordon Geon,” [\*Phys. Rev.\* \*\*172\*\* \(1968\) 1331–1342](#).
- [123] R. Ruffini and S. Bonazzola, “Systems of selfgravitating particles in general relativity and the concept of an equation of state,” [\*Phys. Rev.\* \*\*187\*\* \(1969\) 1767–1783](#).

- [124] E. Seidel and W. M. Suen, “Oscillating soliton stars,” [Phys. Rev. Lett. \*\*66\*\* \(1991\) 1659–1662](#).
- [125] L. Visinelli, “Boson stars and oscillatons: A review,” [Int. J. Mod. Phys. D \*\*30\*\* no. 15, \(2021\) 2130006](#), [[2109.05481](#)].
- [126] I. I. Tkachev, “On the possibility of Bose star formation,” [Phys. Lett. B \*\*261\*\* \(1991\) 289–293](#).
- [127] D. G. Levkov, A. G. Panin, and I. I. Tkachev, “Gravitational Bose-Einstein condensation in the kinetic regime,” [Phys. Rev. Lett. \*\*121\*\* no. 15, \(2018\) 151301](#), [[1804.05857](#)].
- [128] B. Eggemeier and J. C. Niemeyer, “Formation and mass growth of axion stars in axion miniclusters,” [Phys. Rev. D \*\*100\*\* no. 6, \(2019\) 063528](#), [[1906.01348](#)].
- [129] A. S. Dmitriev, D. G. Levkov, A. G. Panin, and I. I. Tkachev, “Self-similar growth of Bose stars,” [[2305.01005](#)].
- [130] D. G. Levkov, A. G. Panin, and I. I. Tkachev, “Radio-emission of axion stars,” [Phys. Rev. D \*\*102\*\* no. 2, \(2020\) 023501](#), [[2004.05179](#)].
- [131] J. H. Buckley, P. S. B. Dev, F. Ferrer, and F. P. Huang, “Fast radio bursts from axion stars moving through pulsar magnetospheres,” [Phys. Rev. D \*\*103\*\* no. 4, \(2021\) 043015](#), [[2004.06486](#)].
- [132] T. D. P. Edwards, B. J. Kavanagh, L. Visinelli, and C. Weniger, “Transient Radio Signatures from Neutron Star Encounters with QCD Axion Miniclusters,” [Phys. Rev. Lett. \*\*127\*\* no. 13, \(2021\) 131103](#), [[2011.05378](#)].
- [133] M. A. Amin, A. J. Long, Z.-G. Mou, and P. Saffin, “Dipole radiation and beyond from axion stars in electromagnetic fields,” [JHEP \*\*06\*\* \(2021\) 182](#), [[2103.12082](#)].
- [134] Y. Bai, X. Du, and Y. Hamada, “Diluted axion star collisions with neutron stars,” [JCAP \*\*01\*\* no. 01, \(2022\) 041](#), [[2109.01222](#)].
- [135] A. Iwazaki, “Radiation burst by axion star collision with star in the Andromeda Galaxy,” [Phys. Lett. B \*\*829\*\* \(2022\) 137089](#), [[2203.07579](#)].
- [136] S. J. Witte, S. Baum, M. Lawson, M. C. D. Marsh, A. J. Millar, and G. Salinas, “Transient radio lines from axion miniclusters and axion stars,” [Phys. Rev. D \*\*107\*\* no. 6, \(2023\) 063013](#), [[2212.08079](#)].
- [137] P. J. Fox, N. Weiner, and H. Xiao, “Recurrent Axinovae and their Cosmological Constraints,” [[2302.00685](#)].
- [138] M. Escudero, C. K. Pooni, M. Fairbairn, D. Blas, X. Du, and D. J. E. Marsh, “Axion Star Explosions: A New Source for Axion Indirect Detection,” [[2302.10206](#)].
- [139] V. Dandoy, J. Jaeckel, and V. Montoya, “Using Axion Miniclusters to Disentangle the Axion-photon Coupling and the Dark Matter Density,” [[2307.11871](#)].
- [140] P. H. Chavanis and L. Delfini, “Mass-radius relation of Newtonian self-gravitating Bose-Einstein condensates with short-range interactions: II. Numerical results,” [Phys. Rev. D \*\*84\*\* \(2011\) 043532](#), [[1103.2054](#)].
- [141] J. L. Spitzer, “The stability of isolated clusters,” [Mon. Not. Roy. Astron. Soc. \*\*100\*\* \(1940\) 396](#).
- [142] S. Chandrasekhar, “Dynamical Friction. I. General Considerations: the Coefficient of Dynamical Friction,” [Astrophys. J. \*\*97\*\* \(1943\) 255](#).

- [143] J. L. Spitzer, “Equipartition and the formation of compact nuclei in spherical stellar systems,” [\*Astrophys. J.\* \*\*158\*\* \(1969\) L139](#).
- [144] D. Merritt, “Dynamics and evolution of galactic nuclei,” [Princeton University Press](#) (2013) .
- [145] G. Battaglia, A. Helmi, H. Morrison, P. Harding, E. W. Olszewski, M. Mateo, K. C. Freeman, J. Norris, and S. A. Sheiman, “The Radial velocity dispersion profile of the Galactic Halo: Constraining the density profile of the dark halo of the Milky Way,” [\*Mon. Not. Roy. Astron. Soc.\* \*\*364\*\* \(2005\) 433–442](#), [[astro-ph/0506102](#)]. [Erratum: *Mon. Not. Roy. Astron. Soc.* 370, 1055 (2006)].
- [146] W. R. Brown, M. J. Geller, S. J. Kenyon, and A. Diaferio, “Velocity Dispersion Profile of the Milky Way Halo,” [\*Astron. J.\* \*\*139\*\* \(2010\) 59](#), [[0910.2242](#)].
- [147] T. D. Brandt, “Constraints on MACRO Dark Matter from Compact Stellar Systems in Ultra-Faint Dwarf Galaxies,” [\*Astrophys. J. Lett.\* \*\*824\*\* no. 2, \(2016\) L31](#), [[1605.03665](#)].
- [148] **GRAVITY** Collaboration, R. Abuter et al., “A geometric distance measurement to the Galactic center black hole with 0.3% uncertainty,” [\*Astron. Astrophys.\* \*\*625\*\* \(2019\) L10](#), [[1904.05721](#)].
- [149] R. Ekers and T. L. Wilson, “**Radio Telescopes**,” in *Planets, Stars and Stellar Systems. Volume 1: Telescopes and Instrumentation*, T. D. Oswalt and I. S. McLean, eds., p. 315. 2013.
- [150] P. E. Dewdney, P. J. Hall, R. T. Schilizzi, and T. J. L. W. Lazio, “The square kilometre array,” [\*Proc. IEEE\* \*\*97\*\* no. 8, \(2009\) 1482–1496](#).
- [151] R. Braun, “Ska1 imaging science performance,” [Document number SKA-TEL-SKO-DD-XXX Revision A Draft 2](#) (2014) .
- [152] R. Braun, T. Bourke, J. Green, E. Keane, and J. Wagg, “Ska1 level 0 science requirements,” [SKA-TEL-SKO-0000007-Rev02](#) (2015) .
- [153] SKAO, “The ska telescopes.” <https://www.skao.int/index.php/en>, 2023. [Online; accessed 18-October-2023].
- [154] P. Jiang et al., “Commissioning progress of the FAST,” [\*Sci. China Phys. Mech. Astron.\* \*\*62\*\* no. 5, \(2019\) 959502](#), [[1903.06324](#)].
- [155] C. Ajello, G. Bonelli, and G. Sironi, “Evaluation of earth’s atmospheric brightness temperature at decimetric wavelengths,” [\*Astrophys. J. Suppl. Ser.\* \*\*96\*\* \(1995\) 643–650](#).
- [156] **HAYSTAC** Collaboration, K. M. Backes et al., “A quantum-enhanced search for dark matter axions,” [\*Nature\* \*\*590\*\* no. 7845, \(2021\) 238–242](#), [[2008.01853](#)].
- [157] **HAYSTAC** Collaboration, M. J. Jewell et al., “New results from HAYSTAC’s phase II operation with a squeezed state receiver,” [\*Phys. Rev. D\* \*\*107\*\* no. 7, \(2023\) 072007](#), [[2301.09721](#)].
- [158] A. P. Quiskamp, B. T. McAllister, P. Altin, E. N. Ivanov, M. Goryachev, and M. E. Tobar, “Direct search for dark matter axions excluding ALPogenesis in the 63- to 67- $\mu$ eV range with the ORGAN experiment,” [\*Sci. Adv.\* \*\*8\*\* no. 27, \(2022\) abq3765](#), [[2203.12152](#)].
- [159] C. A. Thomson, B. T. McAllister, M. Goryachev, E. N. Ivanov, and M. E. Tobar, “Upconversion Loop Oscillator Axion Detection Experiment: A Precision Frequency Interferometric Axion Dark Matter Search with a Cylindrical Microwave Cavity,” [\*Phys. Rev. Lett.\* \*\*126\*\* no. 8, \(2021\) 081803](#), [[1912.07751](#)]. [Erratum: *Phys. Rev. Lett.* 127, 019901 (2021)].

- [160] S. De Panfilis, A. C. Melissinos, B. E. Moskowitz, J. T. Rogers, Y. K. Semertzidis, W. Wuensch, H. J. Halama, A. G. Prodehl, W. B. Fowler, and F. A. Nezrick, “Limits on the Abundance and Coupling of Cosmic Axions at  $4.5\text{-}\mu\text{eV} < m(a) < 5.0\text{-}\mu\text{eV}$ ,” [\*Phys. Rev. Lett.\* \*\*59\*\* \(1987\) 839](#).
- [161] W. Wuensch, S. De Panfilis-Wuensch, Y. K. Semertzidis, J. T. Rogers, A. C. Melissinos, H. J. Halama, B. E. Moskowitz, A. G. Prodehl, W. B. Fowler, and F. A. Nezrick, “Results of a Laboratory Search for Cosmic Axions and Other Weakly Coupled Light Particles,” [\*Phys. Rev. D\* \*\*40\*\* \(1989\) 3153](#).
- [162] C. Hagmann, P. Sikivie, N. S. Sullivan, and D. B. Tanner, “Results from a search for cosmic axions,” [\*Phys. Rev. D\* \*\*42\*\* \(1990\) 1297–1300](#).
- [163] **CAPP** Collaboration, O. Kwon et al., “First Results from an Axion Haloscope at CAPP around  $10.7\text{ }\mu\text{eV}$ ,” [\*Phys. Rev. Lett.\* \*\*126\*\* no. 19, \(2021\) 191802, \[2012.10764\]](#).
- [164] Y. Lee, B. Yang, H. Yoon, M. Ahn, H. Park, B. Min, D. Kim, and J. Yoo, “Searching for Invisible Axion Dark Matter with an 18 T Magnet Haloscope,” [\*Phys. Rev. Lett.\* \*\*128\*\* no. 24, \(2022\) 241805, \[2206.08845\]](#).
- [165] J. Kim et al., “Near-Quantum-Noise Axion Dark Matter Search at CAPP around  $9.5\text{ }\mu\text{eV}$ ,” [\*Phys. Rev. Lett.\* \*\*130\*\* no. 9, \(2023\) 091602, \[2207.13597\]](#).
- [166] A. K. Yi et al., “Axion Dark Matter Search around  $4.55\text{ }\mu\text{eV}$  with DFSZ Sensitivity,” [\*Phys. Rev. Lett.\* \*\*130\*\* no. 7, \(2023\) 071002, \[2210.10961\]](#).
- [167] B. Yang, H. Yoon, M. Ahn, Y. Lee, and J. Yoo, “Extended Axion Dark Matter Search Using the CAPP18T Haloscope,” [\*Phys. Rev. Lett.\* \*\*131\*\* no. 8, \(2023\) 081801, \[2308.09077\]](#).
- [168] C. M. Adair et al., “Search for Dark Matter Axions with CAST-CAPP,” [\*Nature Commun.\* \*\*13\*\* no. 1, \(2022\) 6180, \[2211.02902\]](#).
- [169] D. Alesini et al., “Search for invisible axion dark matter of mass  $m_a = 43\text{ }\mu\text{eV}$  with the QUAX- $a\gamma$  experiment,” [\*Phys. Rev. D\* \*\*103\*\* no. 10, \(2021\) 102004, \[2012.09498\]](#).
- [170] D. Alesini et al., “Search for Galactic axions with a high-Q dielectric cavity,” [\*Phys. Rev. D\* \*\*106\*\* no. 5, \(2022\) 052007, \[2208.12670\]](#).
- [171] J. A. Devlin et al., “Constraints on the Coupling between Axionlike Dark Matter and Photons Using an Antiproton Superconducting Tuned Detection Circuit in a Cryogenic Penning Trap,” [\*Phys. Rev. Lett.\* \*\*126\*\* no. 4, \(2021\) 041301, \[2101.11290\]](#).
- [172] **TASEH** Collaboration, H. Chang et al., “First Results from the Taiwan Axion Search Experiment with a Haloscope at  $19.6\text{ }\mu\text{eV}$ ,” [\*Phys. Rev. Lett.\* \*\*129\*\* no. 11, \(2022\) 111802, \[2205.05574\]](#).
- [173] Y. Sun, K. Schutz, H. Sewalls, C. Leung, and K. W. Masui, “Looking in the axion mirror: An all-sky analysis of stimulated decay,” [\*\[2310.03788\]\*](#).
- [174] E. Todarello, F. Calore, and M. Regis, “Anatomy of astrophysical echoes from axion dark matter,” [\*\[2311.00051\]\*](#).
- [175] I. I. Tkachev, “Coherent scalar field oscillations forming compact astrophysical objects,” [\*Sov. Astron. Lett.\* \*\*12\*\* \(1986\) 305–308](#).
- [176] I. I. Tkachev, “An Axionic Laser in the Center of a Galaxy?,” [\*Phys. Lett. B\* \*\*191\*\* \(1987\) 41–45](#).

- [177] T. W. Kephart and T. J. Weiler, “Stimulated radiation from axion cluster evolution,” [Phys. Rev. D](#) **52** (1995) 3226–3238.
- [178] S. L. Adler, “Axial vector vertex in spinor electrodynamics,” [Phys. Rev.](#) **177** (1969) 2426–2438.